

Learning Legged MPC with Smooth Neural Surrogates

Samuel A. Moore¹, Easop Lee², and Boyuan Chen^{1,2,3}

Abstract—Deep learning and model predictive control (MPC) can play complementary roles in legged robotics. However, integrating learned models with online planning remains challenging. When dynamics are learned with neural networks, three key difficulties arise: (1) stiff transitions from contact events may be inherited from the data; (2) additional non-physical local nonsmoothness can occur; and (3) training datasets can induce non-Gaussian model errors due to rapid state changes. We address (1) and (2) by introducing the *smooth neural surrogate*, a neural network with tunable smoothness designed to provide informative predictions and derivatives for trajectory optimization through contact. To address (3), we train these models using a heavy-tailed likelihood that better matches the empirical error distributions observed in legged-robot dynamics. Together, these design choices substantially improve the reliability, scalability, and generalizability of learned legged MPC. Across zero-shot locomotion tasks of increasing difficulty, smooth neural surrogates with robust learning yield consistent reductions in cumulative cost on simple, well-conditioned behaviors (typically $\approx 10\text{--}50\%$), while providing substantially larger gains in regimes where standard neural dynamics often fail outright. In these regimes, smoothing enables reliable execution (0/5 \rightarrow 5/5 success) and produces $\approx 2\text{--}50\times$ lower cumulative cost, reflecting orders-of-magnitude absolute improvements in robustness rather than incremental performance gains. More information and video demonstrations can be found at <https://generalroboticslab.com/SNS-MPC>

Index Terms—Reinforcement Learning, Model Predictive Control, Legged Robots, Neural Networks, Contact Dynamics

I. INTRODUCTION

REINFORCEMENT learning (RL) and model predictive control have both seen widespread success in legged robotics. Learning provides strong representational flexibility and scalability, particularly through techniques such as domain randomization, enabling capabilities like blind locomotion over challenging terrain [1], [2]. Model predictive control, by contrast, enables online behavior shaping by adjusting costs and constraints, making it well suited for rapid task switching without retraining [3], [4]. Despite these complementary strengths, the effectiveness of MPC within an RL pipeline remains limited for legged robots, and existing controllers tend to favor either learned policies with limited flexibility or scenario-specific analytic models with limited generalization or scalability.

Learned MPC, which combines learned dynamics with online planning, offers a promising middle ground. However, improving the prediction error of neural dynamics does not guarantee improved control performance [5]. Even exact analytic models can perform poorly when contact dynamics are not handled appropriately within the optimization [6]–[8].

¹Department of Mechanical Engineering and Materials Science, Duke University, Durham, NC, USA.

²Department of Electrical and Computer Engineering, Duke University, Durham, NC, USA.

³Department of Computer Science, Duke University, Durham, NC, USA.

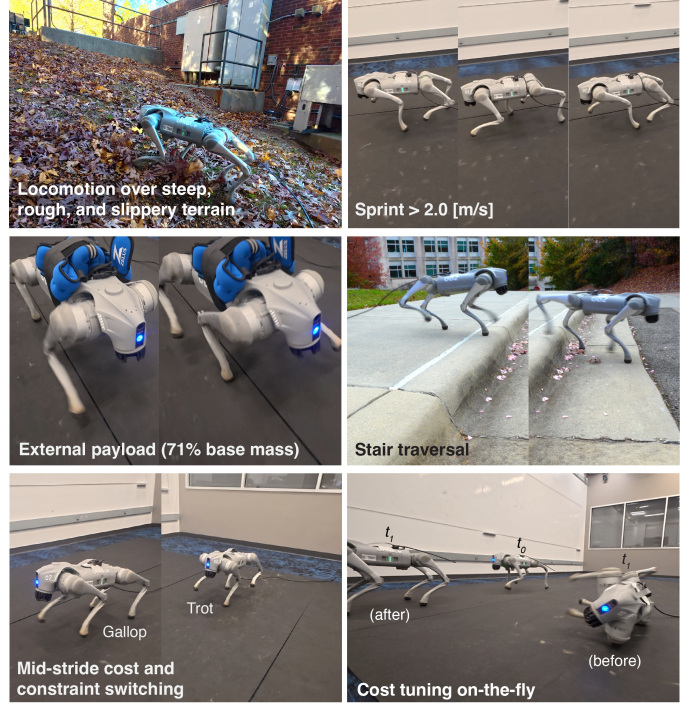


Fig. 1. Learning model predictive control and state estimation for legged robots. Stiff legged-robot dynamics, when modeled with standard neural networks, introduce nonsmooth behavior that destabilizes learning and MPC. Motivated by smooth approximations of nonsmooth functions and by robust optimization, we introduce a neural architecture and a heavy-tailed likelihood that provides stable learning and informative gradients through contact events. Our smooth neural surrogates learn terrain-varying dynamics and state estimation while generalizing to new tasks at test time with MPC. Together, they combine the representational flexibility of deep learning with the task-level adaptability of MPC, enabling reliable whole-body control across diverse behaviors and environments.

Our starting point is a simple but important observation: *the pathologies of optimization under contact dynamics, particularly for gradient-based methods, are compounded when the dynamics are modeled with standard neural networks.* We hypothesize that these failures are driven primarily by nonsmoothness, which manifests in three ways:

- 1) Neural network dynamics often inherit the very stiff transitions present in the ground-truth contact dynamics, making these models difficult to optimize through.
- 2) Neural networks frequently introduce additional local nonsmoothness and, consequently, local optima that do not exist in the underlying physical dynamics.
- 3) Training datasets for these stiff dynamics necessarily contain rapid state changes, which can destabilize learning and violate common Gaussian noise assumptions.

A promising direction for addressing 1) and 2) is to explicitly control neural network smoothness. Smooth archi-

Learned MPC with smooth neural surrogates

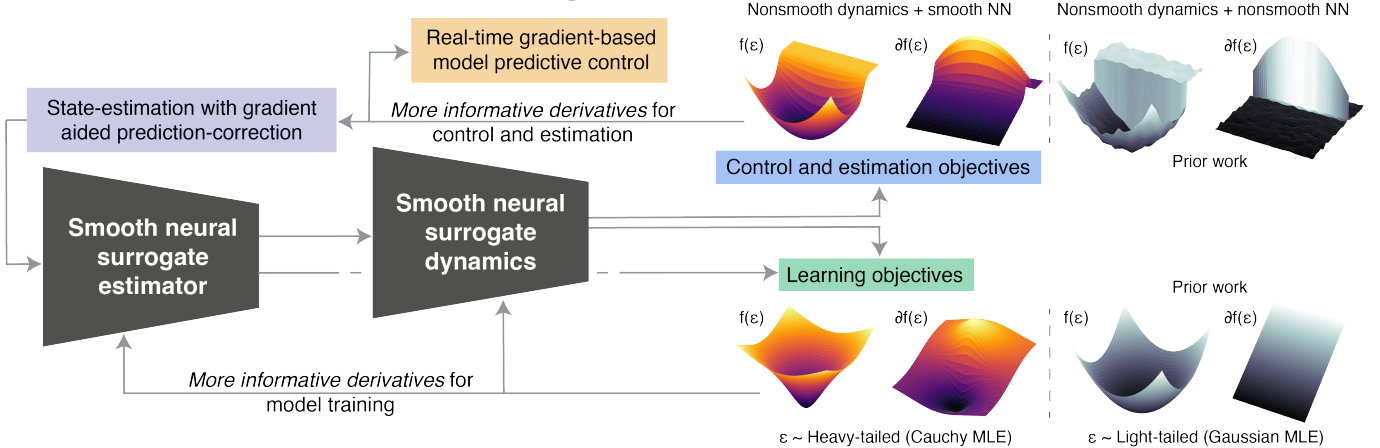


Fig. 2. **Our framework for learning generalizable MPC and state estimation.** The backbone of our method consists of dynamics and estimator modules with an architecture we introduce called the *smooth neural surrogate*. The smooth neural surrogate is an MLP provides informative derivatives for planning and state estimation, even in the presence of nonsmooth dynamics and out-of-distribution data. To combat impulse-like residuals in the learned dynamics and estimation, we train both modules via Cauchy maximum-likelihood estimation (MLE). Finally, we introduce a gray-box model predictive controller and model-based state-estimation strategy that exploit the smooth derivatives provided by our learned dynamics.

tures and Lipschitz-constrained networks can yield better gradients for test time optimization, improved generalization, and robustness to perturbations [9]–[13]. Yet, these ideas have seen limited use in control and robotics [14], [15], especially for learning stiff legged robot dynamics. The goal of smoothing in this context is not to accurately reproduce discontinuous contact forces, but to provide well-conditioned local approximations that are compatible with optimization.

Addressing 3) requires checking the assumptions behind the loss function and the implied likelihood model. In practice, Gaussian error assumptions are common [5], [16]–[22], but they are often unverified and inappropriate for datasets that introduce heavy-tailed errors, a phenomenon we explicitly observe in legged-robot dynamics. Cauchy noise models are known to perform significantly better when the errors are impulsive in nature [23].

In this paper, we study these pathologies through full-order, single-shooting MPC for legged robots, with both the dynamics and the state estimator learned from scratch. Single shooting is the simplest form of trajectory optimization: an open-loop control sequence $u(t)$ is parameterized over a planning horizon, the dynamics are rolled out forward in time, and an optimizer iteratively updates $u(t)$ to minimize a cost. In principle, this technique can be directly paired with any general-purpose gradient-based optimizer [24]. In practice, however, gradient-based single shooting is notorious for poorly conditioned gradients, sensitivity to local minima, and nonsmoothness. [7], [25]. While sampling-based methods are often preferred in the presence of nonsmoothness [4], [5], [17], [22], [26]–[28], their performance and reliability still depend strongly on the quality and regularity of the learned dynamics. Moreover, although sampling-based MPC can tolerate nonsmooth dynamics, it scales poorly with action dimension and relies on significant compute, motivating gradient-based MPC as a more efficient and scalable alternative if informative derivatives are available. In either case, the simplicity and gen-

erality of gray-box (gradient-based) and black-box (sampling-based) single shooting make them pragmatic choices for neural MPC. They preserve the full representational flexibility of deep learning and impose no assumptions on the dynamics model (rigid-body, Markov, black-box, etc.) or on the structure of the optimization problem (stage-wise costs, constraints, and so on).

This context raises several motivating questions. First, can smooth neural dynamics and heavy-tailed likelihoods improve training stability and enable reliable gradient-based MPC through contact, and what role does each component play in the resulting performance? Second, although sampling-based MPC is often favored under learned neural dynamics, do these same design choices also benefit sampling-based methods, and what advantages remain for gradient-based MPC once smoothness is enforced? Finally, can learned MPC and state estimation for legged robots combine the versatility afforded by domain randomization with the task-level flexibility of MPC?

We answer these questions by extending smooth neural architectures for use as learned dynamics models in MPC through contact. We introduce the *smooth neural surrogate* (SNS): a multilayer perceptron with learned layer-wise Lipschitz constants and a global smoothness budget that constrains first- and/or second-order behavior (Section IV). We pair this architecture with robust maximum-likelihood estimation using heavy-tailed noise models, which better match the empirical error distribution observed in legged-robot dynamics (Section V). We focus on multilayer perceptrons (MLPs) as a controlled setting to isolate the effects of smoothness and robust learning on trajectory optimization, leaving extensions to higher-capacity architectures to future work.

We train both the dynamics and a predictor-corrector state estimator under domain randomization, and deploy the resulting models in a single-shooting MPC framework (Section VI). These learned modules are then transferred to hardware and

evaluated on unseen terrains and tasks without additional training (Fig. 1, Section VI).

II. SYSTEM OVERVIEW AND CONTRIBUTIONS

Fig. 2 provides a high-level overview of our approach to learned, gradient-based MPC for legged robots under domain randomization and partial observability. An SNS-MLP state estimator refines prior state estimates using corrections informed by the learned dynamics. The SNS-MLP dynamics model, in turn, predicts future states based on the refined estimates. Both modules are trained using heavy-tailed (Cauchy) maximum-likelihood estimation. The estimator’s smoothness acts primarily as a regularizer, whereas the dynamics model’s smoothness is explicitly designed to stabilize gradient-based estimation and single-shooting MPC through contact.

Our primary technical contributions are:

- 1) We introduce the smooth neural surrogate (SNS-MLP), a neural network with tunable first- and/or second-order derivatives (Section IV). We show that this architecture yields more informative predictions and derivatives for legged MPC through contact than standard neural baselines (Section VI).
- 2) We demonstrate that dynamics residuals in model-based reinforcement learning for legged robots can exhibit heavy-tailed behavior (Section V), and show that heavy-tailed likelihoods significantly improve training convergence and downstream control performance (Section VI).
- 3) We show that, when paired with appropriately smooth learned dynamics, gradient-based single-shooting MPC can outperform strong sampling-based methods in scalability, convergence, and efficiency, while the same smoothing also improves the performance of sampling-based MPC (Section VI).
- 4) We learn full-order dynamics and state estimation under domain randomization (Section V) and deploy the resulting models on a real quadruped robot, synthesizing new behaviors in unseen environments without additional training (Section VI).

III. RELATED WORK

A. Model-Based Control of Hybrid Systems

Contact dynamics are hybrid, with smooth continuous modes separated by discrete, often non-differentiable transitions. Existing approaches address this either by avoiding gradients altogether or by smoothing to recover informative derivatives.

Sampling-based single-shooting methods exemplify gradient-free approaches. Their popularity stems from ease of implementation and GPU parallelism, with recent advances enabling deployment on quadrupeds using full-order rigid-body models [26], [29]. Much of this progress relies on reducing decision dimensionality through spline-based action parameterizations [4], [26], [29]. Nevertheless, sampling-based MPC remains subject to the curse of dimensionality, heuristic convergence, and high computational cost, and is sensitive to the regularity of the learned dynamics. From a numerical optimization perspective, well-conditioned gradient-based

methods offer the potential for faster convergence, improved scalability, and lower computational overhead [24], [30].

Some gradient-based methods avoid differentiating directly through stiff contact by introducing additional structure, such as optimizing over contact forces or assuming fixed contact modes [6], [7], [28], [31], [32]. Our work is more closely related to approaches that smooth contact dynamics to enable gradient-based planning. Differentiable simulation methods typically achieve this by relaxing complementarity constraints or regularizing contact forces [8], [33]–[37]. While effective, these methods generally rely on analytic, scenario-specific models. More general smoothing strategies, such as randomized smoothing [38], [39], can be applied to arbitrary models, including neural networks, but incur additional computational cost and introduce stochastic gradient noise [34].

Our approach shares the goal of producing well-conditioned gradients for planning, but learns smooth surrogate dynamics directly from data. Similar smoothing principles have been shown to benefit policy learning via differentiable simulation by regularizing contact forces or truncating planning horizons [40]–[42]. Many of the methods above could directly benefit from replacing analytic or learned components with smooth neural surrogates, making them complementary rather than competing approaches.

B. Neural Dynamics

Many learned dynamics approaches rely on model-free RL tools, such as policy gradients or value functions, to enable planning and control [18], [43]–[45]. While effective, these methods limit the task-level flexibility afforded by online trajectory optimization. In learned MPC, black-box neural dynamics are therefore commonly paired with sampling-based optimizers to avoid issues with nonconvexity or poorly conditioned gradients [5], [17], [22], [27], [46], [47]. Diffusion-based planners offer an alternative [44], but still rely on model-free components such as PPO demonstrations for quadruped control [48].

Other works introduce structure through contact-aware or physics-informed priors [20], [49]–[51], reduced-order models and fixed low-level controllers [21], [52], or hybrid simulation-learning pipelines [16], [53]. Our contribution is compatible with these formulations: smooth neural surrogates and heavy-tailed MLE can replace standard neural networks and Gaussian losses without modifying the surrounding optimization problems or priors.

C. Smooth Neural Networks and Robust Optimization

Training to bound a network’s Lipschitz constant has been shown to improve adversarial robustness and generalization [9], [13], [54], [55]. However, many smoothing techniques are either computationally expensive or overly restrictive [10], [12]. Strict 1-Lipschitz methods based on weight orthonormalization [11] can be under-expressive and unstable in practice, while spectral normalization methods are approximate, hyperparameter-sensitive, and incur nontrivial overhead [13], [54]. Liu *et al.* introduced the Lipschitz MLP to address these issues using weight normalization [9]. Our SNS-MLP

extends this approach with a reparameterization that improves convergence and scalability with moderate to large networks under Lipschitz regularization.

In trajectory optimization, Lipschitz-constrained networks have primarily been evaluated in benign, smooth, and low-dimensional settings [15], leaving their effectiveness for high-dimensional, stiff legged-robot dynamics largely unexplored. Although Lipschitz-bounding techniques exist for more expressive architectures [56], we focus on standard MLPs as a controlled setting to isolate the effects of smoothness.

Finally, robust optimization literature has long recognized that Gaussian losses implicitly assume light-tailed noise and finite variance, assumptions that are frequently violated in practice [23], [57]. When residuals are heavy-tailed or impulsive, Gaussian losses overweight outliers, motivating robust alternatives such as Cauchy or Huber losses that reduce their influence [23], [57]–[59]. Despite this, Gaussian error models remain standard when learning dynamics for systems with contact [5], [17], [18], [28].

IV. SMOOTH NEURAL REPRESENTATIONS

A. Preliminaries

Lipschitz continuity. Many general-purpose optimization algorithms rely on *Lipschitz continuity* as a key ingredient in local convergence guarantees and, in practice, its importance to algorithm performance is well known [24]. A function f is c -Lipschitz if small input changes produce proportionally bounded output changes:

$$\|f(a_0) - f(a_1)\|_p \leq c \|a_0 - a_1\|_p, \quad (1)$$

where $\|\cdot\|_p$ is the p -norm and $c \geq 0$ is the *Lipschitz constant*. **Smooth neural networks.** There is no general formula for directly measuring or shaping the Lipschitz constant of an arbitrary analytic function. However, smooth surrogates based on convolution can make a discontinuous function continuously differentiable, providing some qualitative control over smoothness but at the cost of requiring many additional samples at each evaluation point [38], [39].

Neural network architectures, by contrast, follow fixed analytic templates while remaining capable of approximating arbitrary functions, making quantitative assessments of smoothness more tractable. Thus, for neural networks, a more direct and efficient strategy to quantify and shape smoothness is to use the *Lipschitz upper bound*. For a fully connected network, or MLP, with L layers, the Lipschitz upper bound is given by

$$c_{\text{MLP}} \lesssim \prod_{\ell=1}^L \|W^{(\ell)}\|_p, \quad (2)$$

with proportionality determined by the activation functions; for 1-Lipschitz activations (e.g., softplus, tanh), the relation becomes exact. Although this bound is conservative, it provides meaningful quantitative insight into the global smoothness of the network and removes the need for post hoc randomized smoothing. Compared to naive penalization of (2), weight normalization strategies have proven more fruitful [9].

TABLE I
SMOOTH NEURAL SURROGATES QUANTITIES

Term	Definition
c_ℓ	Learned Lipschitz constant of layer ℓ
$c_{\text{MLP}} \lesssim C = \prod_{\ell} c_\ell$	Approx. Lipschitz upper bound
$S = \sum_{\ell} c_\ell \prod_{j < \ell} c_j$	Propagated curvature terms
$d_{\text{MLP}} \lesssim CS$	Approx. Lipschitz upper bound of the Jacobian
c_{ub}	Sensitivity budget
d_{ub}	Curvature budget

B. Smooth Neural Surrogates

Lipschitz-based weight normalization. We base our approach on Liu *et al.* [9], who use a weight normalization layer paired with learned layerwise scalars c_ℓ that parameterize the ∞ -norm of each weight matrix:

$$\begin{aligned} \hat{W}_{ij}^{(\ell)} &= \text{normalization}\left(W_{ij}^{(\ell)}, c_\ell\right), \quad c_\ell > 0, \\ &= \min\left(1, \frac{c_\ell}{\sum_k |W_{ik}^{(\ell)}|}\right) W_{ij}^{(\ell)}. \end{aligned} \quad (3)$$

Here, c_ℓ serves as the learned Lipschitz constant of the ℓ -th layer (ignoring the activation). Liu *et al.* enforce $c_\ell > 0$ using the parameterization $c_\ell = \text{softplus}(\theta_c^{(\ell)})$, where $\theta_c^{(\ell)}$ is the true trainable variable. The training loss is augmented with a global Lipschitz regularization term via the upper bound $\prod_{\ell} c_\ell$.

Scalable parameterization. In practice, the learned layerwise Lipschitz constants c_ℓ are often large at initialization, causing their product to grow exponentially with network depth. This can lead to slow convergence or even collapse when the model is pressured to satisfy strict smoothness constraints. We hypothesize that this issue stems from the parameterization of c_ℓ . To mitigate it, we introduce an exponential parameterization $c_\ell = \exp(\theta_c^{(\ell)})$. The regularization objective now satisfies:

$$\prod_{\ell} \exp(\theta_c^{(\ell)}) = \exp\left(\sum_{\ell} \theta_c^{(\ell)}\right) = \frac{\partial \exp\left(\sum_{\ell} \theta_c^{(\ell)}\right)}{\partial \theta_c^{(\ell)}}. \quad (4)$$

This parameterization is equivalent to learning $\theta_c^{(\ell)} = \log(c_\ell)$, and ensures that its gradient is distributed evenly across layers, regardless of network depth or width. As a result, the optimization does not easily saturate or collapse when enforcing smoothness, even for very smooth or nonsmooth networks.

Lipschitz regularization penalizes only first-order gradient bounds, which is not always sufficient for smoothing. For example, both ReLU and softplus are 1-Lipschitz, yet only softplus has bounded curvature. Motivated by this distinction, we additionally bound the second derivative of the learned network. We define the total Lipschitz bound $C := \prod_{\ell=1}^L c_\ell$ and the propagated terms $S := \sum_{\ell=1}^L c_\ell \prod_{j < \ell} c_j$ which account for curvature. With this notation, the Lipschitz constant of the Jacobian, d_{MLP} , of an L -layer MLP satisfies

$$d_{\text{MLP}} \lesssim CS. \quad (5)$$

We provide proof of this relation in Appendix A.

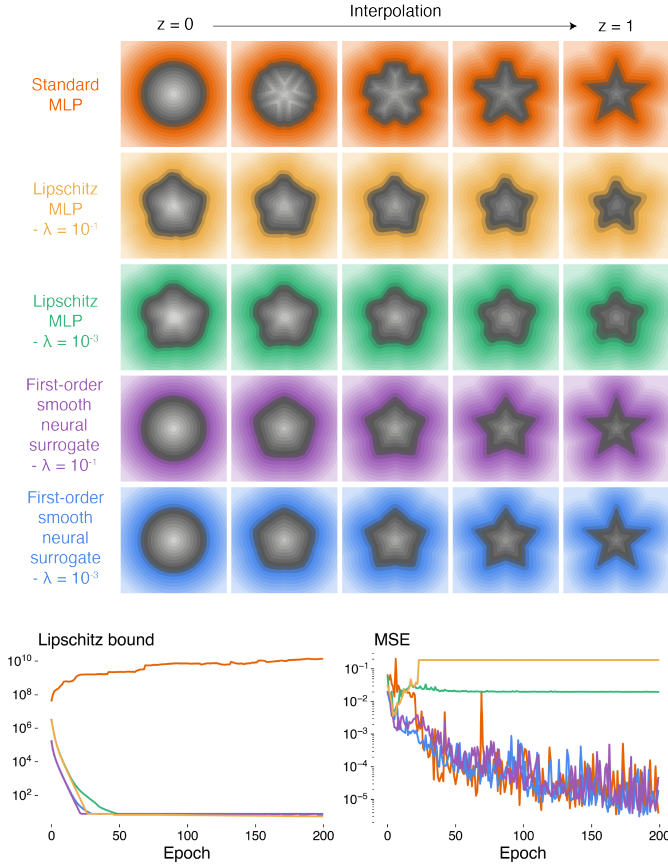


Fig. 3. **Smooth neural surrogates converge under strict Lipschitz constraints and enable zero-shot generalization.** **Top:** Lowest-MSE models for the 2-D shape interpolation task. Only the SNS converges under tight Lipschitz budgets; the Lipschitz MLP [9] collapses. **Middle:** Evolution of Lipschitz upper bounds and training MSE.

Smooth neural surrogate objectives. We define the k -th order SNS objective for $k \in \{1, 2\}$ as

$$\mathcal{L}_k = \mathcal{L}_{\text{main}} + \lambda \max\left(1, \frac{C S^{k-1}}{B_k}\right), \quad (6)$$

where B_k is the corresponding smoothness budget. Rescaling the numerator by B_k (rather than enforcing $\max(C S^{k-1}, B_k)$ directly) ensures that the regularization coefficient λ remains independent of the smoothness scale. Tuning the functions Lipschitz constant controls first-order smoothness (bounded gradient magnitude), while tuning the Jacobian Lipschitz constant is equivalent to bounding the second derivative. For a first-order SNS ($k = 1$) and $B_1 = c_{\text{ub}}$ is the sensitivity budget. Likewise, for a second-order SNS ($k = 2$) and $B_2 = d_{\text{ub}}$ is the curvature budget. Clearly, the second-order objective also bounds first-order behavior, but one could also jointly enforce specific constraints $c_{\text{MLP}} \leq c_{\text{ub}}$ and $d_{\text{MLP}} \leq d_{\text{ub}}$ by using both forms of Eq. (6).

As a guideline, a practitioner may prefer curvature suppression ($k = 2$) in settings where reliable second-order derivatives are needed, for example, Newton-type optimization, physics-informed machine learning, and differentiable optimization or simulation. Table I provides an overview of the SNS quantities for convenience.

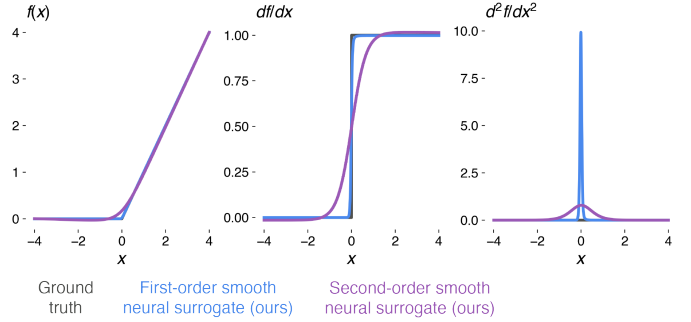


Fig. 4. **First- and second-order smooth neural surrogates for the ReLU function.** First-order surrogates eliminate large jumps but can form cusp-like shapes if trained for longer periods. Second-order surrogates bound curvature throughout training, yielding smooth transitions similar to analytical smooth surrogates like softplus or mish.

C. Experiments and Examples

These experiments are designed to answer the following questions: (1) What do smooth neural surrogates of simple functions look like, and how do they differ from standard MLP approximations? and (2) How does the proposed parameterization of the layerwise constants c_ℓ influence convergence behavior during training? Since our method is a direct extension of Liu et al., who already provide extensive empirical comparisons against alternative smooth neural parameterizations and regularization strategies, we do not seek to re-establish state-of-the-art performance. Accordingly, we restrict our baselines to their Lipschitz MLP and a standard MLP. For the Lipschitz MLP baseline, we train using the SNS objective with $k = 1$ to enable a controlled comparison that isolates the effect of the exponential parameterization of the layerwise Lipschitz constants. All experiments are implemented in JAX, with additional details provided in Appendix B.

Shape interpolation. A key advantage of smooth neural surrogates is their ability to learn globally smooth representations of unknown functions. We evaluate this property on a 2-D shape interpolation task, where the model must interpolate between two shapes given samples only at $z = 0$ and $z = 1$.

The standard MLP fails to produce coherent or continuous interpolation in z (Fig. 3); instead, its intermediate representation has spurious discontinuities. Although prior work reports successful interpolation with Lipschitz MLPs, it collapses under a tight sensitivity budget ($c_{\text{ub}} = 8$), even when the regularization weight is reduced by two orders of magnitude. In contrast, the SNS converges in both smoothness and MSE and consistently reconstructs valid intermediate shapes in a zero-shot manner. From this simple example, it is clear that smoothness can also play a key role in model generalization.

1-D nonsmooth functions. We further study smoothness constraints on a controlled task: learning the ReLU function. This isolates how first- and second-order smooth surrogates regulate slope and curvature. As shown in Fig. 4, first-order surrogates reduce the discontinuity near the kink but can form cusp-like transitions, while second-order surrogates bound curvature and produce smooth transitions similar to analytical surrogates (e.g., softplus, mish). Second-order constraints introduce more bias but provide this additional control.

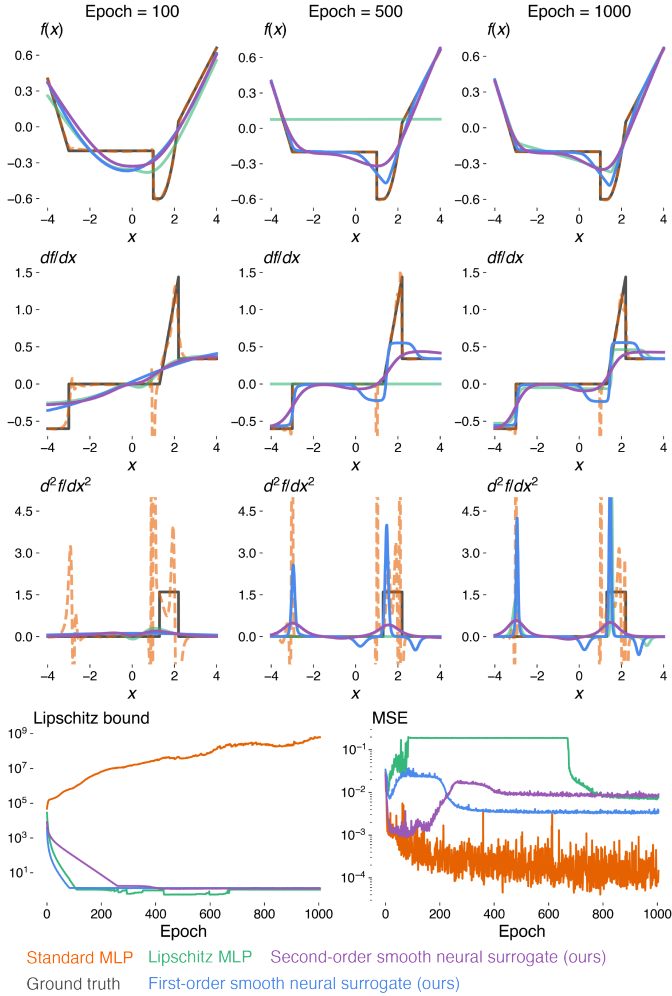


Fig. 5. **Smooth neural surrogates provide informative derivatives throughout training.** **Top:** Learned surrogates for a nonsmooth piecewise function. Standard MLPs develop extremely stiff gradients unsuitable for gradient-based optimization, and Lipschitz MLPs briefly collapse under smoothness constraints. Smooth neural surrogates yield informative derivatives for downstream optimization throughout training. **Bottom:** Evolution of Lipschitz bounds and MSE during training.

We next approximate a 1-D piecewise function (Appendix B) that mimics a hopping robot’s cost landscape [26]. In Fig. 5, the standard MLP fits the data with little bias but yields uninformative gradients, and the Lipschitz MLP again collapses under the constraint. First- and second-order SNS-MLPs converge to stable, slightly biased representations that smooth the discontinuities and nonconvexities; the second-order model adds further bias but has lower curvature.

Smoothing particle-mass contact dynamics. Finally, we evaluate the surrogates on a physical system with stiff contact dynamics: a particle-mass model impacting the ground (Appendix B). Networks are trained to predict next-step position and velocity. Standard MLPs accurately capture zeroth-order behavior but yield erratic, stiff first- and second-order derivatives (Fig. 6). Notably, the MLP’s learned derivatives can be smoother than the ground truth in some instances, consistent with prior observations [20], but are still relatively stiff and noisy. Both SNS-MLP variants model the dynam-

ics while maintaining stable, well-behaved derivatives. Their zeroth-order predictions show minor bias near impact, but the derivatives remain nicely bounded and smooth.

V. LEARNING GENERALIZABLE LEGGED MPC AND STATE ESTIMATION

In the previous section, we showed that standard neural networks are often unreliable as smooth surrogates for nonsmooth functions: they both inherit the nonsmoothness from the training data and introduce additional spurious nonsmoothness, particularly when data are sparse in regions of the input space. To address these limitations, we introduced the smooth neural surrogate MLP, which mitigates such effects through explicit control of global Lipschitz continuity.

In this section, we detail our methodology for scaling these lightweight architectures to quadruped robots and model predictive control under domain randomization and partial observability. The full training procedure is summarized in Algorithm 1, with implementation details provided in the sections that follow and in Appendix C.

A. Preliminaries

Learned MPC. Given states x and actions u , a typical formulation [5], [17] for learned dynamics is

$$x_{t+1} = x_t + d\hat{\mu}_\theta(x_t, u_t)dt + \varepsilon, \quad \varepsilon \sim P, \quad (7)$$

where P denotes an unspecified residual or error distribution. It is common to train the dynamics with one-step or multi-step Gaussian losses. It is also standard for the dynamics to depend on a history of states and actions $(x_{t-H:t}, u_{t-H:t})$ to improve accuracy or compensate for partial observability [16], [22], [60].

As noted earlier, we formulate the MPC problem as a single-shooting optimization over an action sequence $u_{0:T-1}$ with horizon T . The controller minimizes a cost function ℓ under inequality constraints g_i , using differentiable roll-outs (forward simulation) of the learned dynamics, where $x_{1:T} = \text{rollout}_\theta(u_{0:T-1})$. We note that equality constraints can always be expressed as paired inequalities. The resulting optimization problem is

$$\begin{aligned} \min_{u_{0:T-1}} \quad & \ell(\text{rollout}_\theta(u_{0:T-1}), u_{0:T-1}) \\ \text{s.t.} \quad & 0 \geq g_i(\text{rollout}_\theta(u_{0:T-1}), u_{0:T-1}). \end{aligned} \quad (8)$$

We compare two methods for solving (8): a state-of-the-art sampling-based method, DIAL-MPC [26], and our gradient-based generalized Gauss-Newton method (GGN-MPC). The optimization is vectorized across environments using `vmap`(·). **Learned state estimation.** Since legged robots operate under partial observability, we need state estimation in order to use the learned dynamics for MPC. Classical estimators for legged robots, such as Kalman or particle-filter variants, often rely on accurate contact information, prior gait knowledge, or rigid-body assumptions, and they can become unreliable on varied terrain [61]–[63]. Although learned state estimation is increasingly common, most concurrent learning for estimation and control in legged robots appears in model-free RL

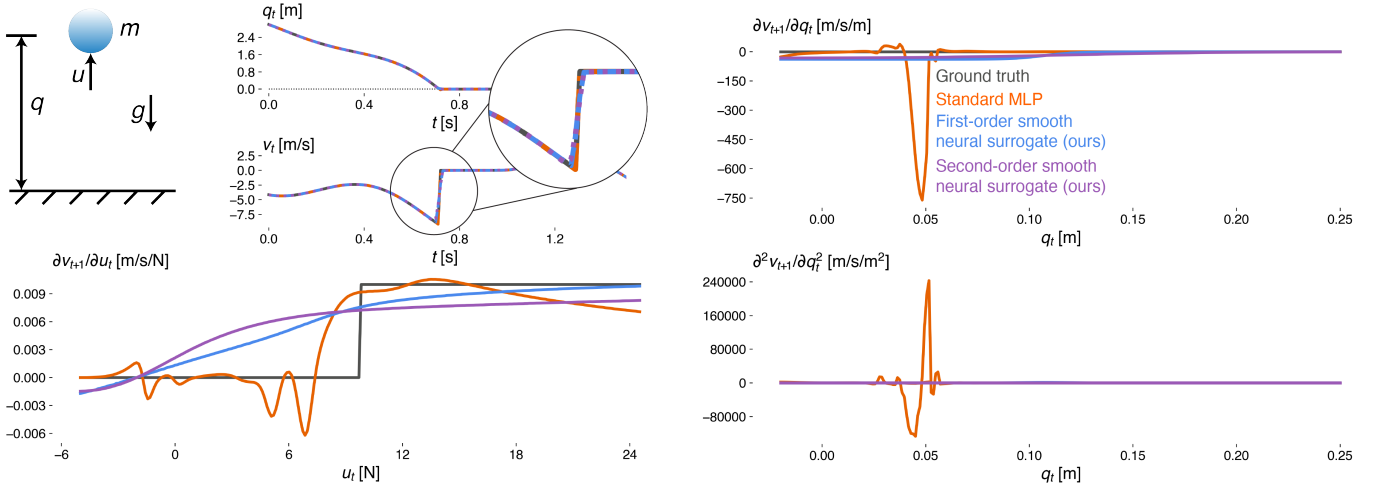


Fig. 6. **Smooth neural surrogates learn contact dynamics while preventing exploding gradients.** **Left:** Learned dynamics for a particle–mass impact model. **Right:** First- and second-order derivatives of the learned models when the mass is sitting on the surface (∂u_t) or traveling at -5 meters per second (∂q_t). Standard MLPs exhibit erratic, stiff gradients, whereas the SNS-MLPs’ gradients are stable and attenuated.

Algorithm 1 Learning legged MPC and state estimation with smooth neural surrogates

Require: Replay buffer \mathcal{D} ; smoothness budgets; horizon T ; history length H ; episode length T_{episode} ; domain randomization, command, and state reset distributions; actuator net A_ψ

- 1: Initialize SNS dynamics model $\hat{\mu}_\theta$, SNS estimator $\hat{\mu}_\phi$, and simulator
- 2: Compute median and MAD over initial \mathcal{D} to set dispersion $\hat{\Sigma}_{\mathcal{D}}$
- 3: **while** training not converged **do**
- 4: **for** each environment instance **do**
- 5: Randomize domain (dynamics, terrain, kinematics, etc.)
- 6: Randomize agent commands and robot state x_0
- 7: Reset episode buffer
- 8: **for** $t = 0$ to T_{episode} **do**
- 9: **if** $t > H$ **then**
- 10: Estimate current state history $\bar{X}_{t|t}$ via $\hat{\mu}_\phi$
- 11: Solve MPC (Eq. (8)) via our generalized Gauss-Newton solver (Section V) and $\hat{\mu}_\theta$
- 12: Set u_t to first element in optimal action trajectory
- 13: **else**
- 14: Set u_t to nominal action (Appendix C)
- 15: **end if**
- 16: Step simulator via u_t , and A_ψ (Appendix C) for x_{t+1}, y_{t+1}
- 17: Store (x_t, u_t, y_t) into replay buffer \mathcal{D}
- 18: **end for**
- 19: **end for**
- 20: **for** each training iteration **do**
- 21: Sample trajectory batch $\{x_t, u_t, y_t\}_{t=0}^{T+H} \sim \mathcal{D}$
- 22: Update θ via Algorithm 2
- 23: Update ϕ via Algorithm 3
- 24: **end for**
- 25: **end while**
- 26: Deploy MPC with learned dynamics and estimation in new environments with new costs and constraints

[63], [64]. Other approaches to neural state estimation take inspiration directly from classical estimators and exploit model predictions [65].

Heavy-tailed maximum likelihood estimation. Although Gaussian error models, implemented through common objectives such as MSE, are a reasonable default. In our setting, we observe that the Cauchy distribution, which is also bell-shaped but heavy-tailed, better reflects the empirical residuals (Fig. 7). The Cauchy distribution is the canonical example of a “pathological” distribution. Unlike the Gaussian, the

TABLE II
1D CAUCHY AND GAUSSIAN RESIDUAL MODELS

Model	Assumption	Gradient	μ	σ
Gaussian	Light tails	$\propto \varepsilon$	Mean	STD
Cauchy	Heavy tails	$\propto \varepsilon/(1 + \varepsilon^2)$	Median	MAD

Cauchy distribution has no finite mean or variance and samples from this distribution over time are described as “jumps” or “impulses”, not unlike transitions in hybrid dynamics.

If we assume $\varepsilon \sim \mathcal{C}(x; \mu, \Sigma)$, we want to minimize any loss proportional to the *Cauchy negative log-likelihood* during training. In the n -dimensional case:

$$-\log \mathcal{C}(x; \mu, \Sigma) = \frac{n+1}{2} \log(1 + (x - \mu)^\top \Sigma^{-1} (x - \mu)) + \frac{1}{2} \log |\Sigma| + \text{const.}, \quad (9)$$

which follows from a special case of the Student’s t-density. The parameter μ defines the *location*, while Σ acts as a *dispersion* term controlling scale along each direction. In the isotropic case $\Sigma = \sigma^2 I$, the location coincides with the median, and the dispersion parameter σ is proportional to the median absolute deviation (MAD) from the median.

Variants of the Cauchy likelihood automatically rescale gradients when compared to Gaussian objectives as shown in Table II; which compares the 1D likelihood models for convenience. For small errors, both behave quadratically. For large errors, the Cauchy gradient saturates, preventing instability and reducing the impact of large ε . For cases where the impulse like dynamics are easy to predict, like our particle-mass example, the two losses will likely perform similarly due to this comparability under small ε .

B. Partially Observable Dynamics and State Estimation

Learned dynamics. We categorize all quantities into measurements y_t (e.g., linear acceleration), state variables x_t used in control (e.g., velocity), and unmeasured environmental factors

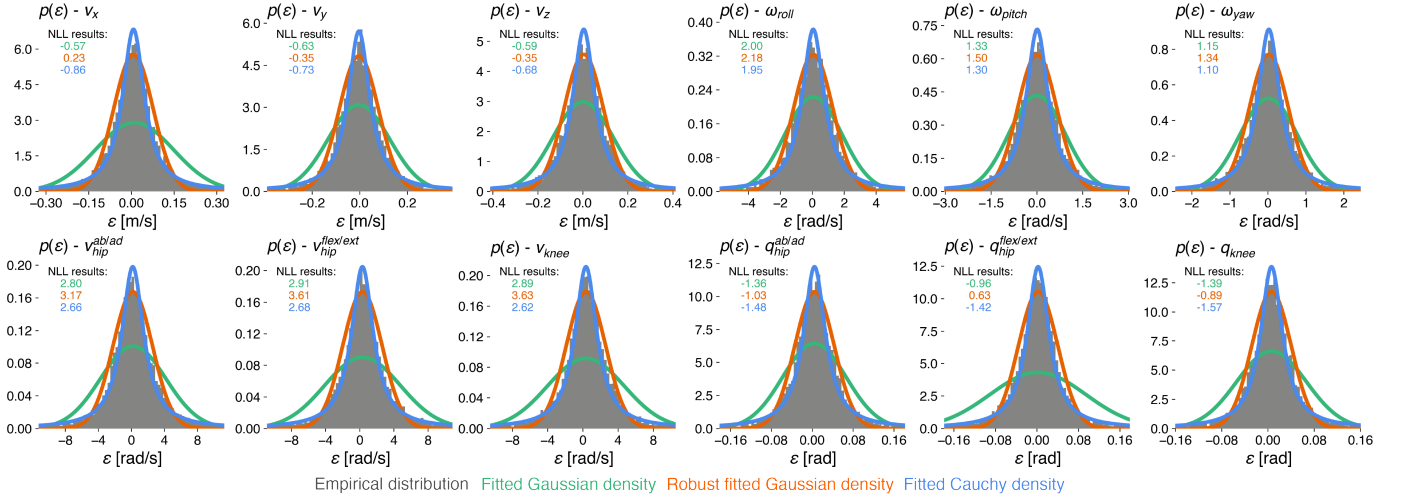


Fig. 7. **Errors for learned quadruped dynamics follow a heavy-tailed Cauchy distribution.** Empirical one-step prediction residuals ε across representative quadruped state variables. Residuals computed from the replay buffer align more closely with a Cauchy density (lower NLL) than with a Gaussian, even when the latter is fit using robust estimators. This suggests that Gaussian losses, such as MSE, are poorly suited for learning legged robot dynamics. Robust Gaussian estimates exploit the identity that, for a true Gaussian, the mean equals the median and $\text{STD} \approx 1.4826 \text{ MAD}$.



Fig. 8. **A simple strategy for whole-body and terrain-aware planning with learned MPC.** By augmenting the states in our neural dynamics model with signed distances from the robot to the terrain, the controller can plan using both classical generalized coordinates and spatial relationships between the body and environment. Training with randomized terrain inclines makes the state estimates and plans robust to uneven ground, varying slopes, and stepped terrain in the real world. Even on sloped, slippery ground with deep debris, the model demonstrates precise awareness of collision geometry and contact dynamics, allowing it to regain footing after a fall.

z_t (e.g., friction). The effect of z_t is captured implicitly through time-delay embedding. Let

$$X_t := x_{t-H:t}, \quad U_t := u_{t-H:t}, \quad (10)$$

denote fixed-length state and action histories. The dynamics modify (7) as

$$x_{t+1} = x_t + d\hat{\mu}_\theta(X_t, U_t) dt + \varepsilon, \quad \varepsilon \sim \mathcal{C}(0, \hat{\Sigma}) \\ \approx \hat{\mu}_\theta(X_t, U_t) \quad (11)$$

Learned estimator (predictor–corrector). Because the dynamics depend on histories, the estimator must maintain a history estimate defined as:

$$\bar{X}_{t|t-1} := \bar{x}_{t-H:t|t-1}, \quad \bar{X}_{t|t} := \bar{x}_{t-H:t|t}, \quad (12)$$

where $\bar{X}_{t|t-1}$ is the prior (predicted) history and $\bar{X}_{t|t}$ is the posterior (corrected) history.

Prediction step. The estimator rolls its previous posterior one step forward using the learned dynamics:

$$\bar{X}_{t|t-1} = \text{roll}(\bar{X}_{t-1|t-1}, \hat{\mu}_\theta(\bar{X}_{t-1|t-1}, U_{t-1})), \quad (13)$$

where $\text{roll}(a, b)$ discards the oldest element of a and appends b . Measurements are predicted via the prior and a typical measurement model, then used to calculate the innovation:

$$\hat{y}_t = h(\bar{X}_{t|t-1}), \quad \nu_t = y_t - \hat{y}_t. \quad (14)$$

Then, the gradient of the total squared innovation provides sensitivities for the neural estimator:

$$g_{\nu, t} = \begin{bmatrix} \frac{\partial(\nu_t^\top \nu_t)}{\partial \bar{X}_{t-1|t-1}} & \frac{\partial(\nu_t^\top \nu_t)}{\partial U_{t-1}} \end{bmatrix}^\top. \quad (15)$$

Algorithm 2 Dynamics training step

Require: Trajectory batch $\{x_t, u_t, y_t\}_{t=0}^{T+H} \sim \mathcal{D}$, initial state estimate covariance $\Sigma_{\bar{x}}$, measurement noise, dynamics smoothness budget \hat{c}_{ub} , horizon T , history length H , SNS dynamics $\hat{\mu}_\theta$, SNS estimator $\hat{\mu}_\zeta$, discount factor γ , learning rate α_0 , loss weights $\lambda_0, \lambda_1, \lambda_2$, and λ_3

- 1: Perturb initial state history estimate $\bar{X}_{t|t} \sim \mathcal{N}(X_t, \Sigma_{\bar{x}})$
 - 2: **for** $t = H$ to $T + H$ **do**
 - 3: Predict x_{t+1} via $\hat{\mu}_\theta$ with X_t, U_t for $\mathcal{L}_{\text{step}}$ (Eq. (19))
 - 4: **if** $t > H$ **then**
 - 5: Predict x_{t+1} via $\hat{\mu}_\theta$ with \hat{X}_t, U_t for $\mathcal{L}_{\text{rollout}}$ (Eq. (20))
 - 6: Predict x_{t+1} via $\hat{\mu}_\theta$ with $\text{sg}(\bar{X}_{t|t}), U_t$ for $\mathcal{L}_{\text{corrupt}}$ (Eq. (21)) and prior $\bar{X}_{t+1|t}$ (Eq. (13))
 - 7: **end if**
 - 8: Corrupt y_t with noise
 - 9: Compute ν_{t+1} (Eq. (14)) and $g_{\nu, t+1}$ (Eq. (15))
 - 10: Estimate $\bar{X}_{t+1|t+1}$ via $\hat{\mu}_\phi$ with $\bar{X}_{t+1|t}, U_t, Y_{t+1}, \nu_{t+1}, g_{\nu, t+1}$
 - 11: **end for**
 - 12: Update θ using total SNS dynamics loss (Eq. (17)) and α_0
-

Algorithm 3 Estimator training step

Require: Trajectory batch $\{x_t, u_t, y_t\}_{t=0}^{T+H} \sim \mathcal{D}$, Initial state estimate covariance $\Sigma_{\bar{x}}$, measurement noise, estimator smoothness budget \hat{c}_{ub} , horizon T , history length H , SNS dynamics $\hat{\mu}_\theta$, SNS estimator $\hat{\mu}_\zeta$, learning rate α_1 , loss weight λ_4

- 1: Perturb initial state history estimate $\bar{X}_{t|t} \sim \mathcal{N}(X_t, \Sigma_{\bar{x}})$
 - 2: **for** $t = H + 1$ to $T + H$ **do**
 - 3: Predict x_{t+1} via $\hat{\mu}_\theta$ with $\text{sg}(\bar{X}_{t|t}), U_t$ for prior $\bar{X}_{t+1|t}$ (Eq. (13))
 - 4: Corrupt y_t with noise
 - 5: Compute ν_{t+1} (Eq. (14)) and $g_{\nu, t}$ (Eq. (15))
 - 6: Estimate $\bar{X}_{t+1|t+1}$ via $\hat{\mu}_\phi$ with $\bar{X}_{t+1|t}, U_t, Y_{t+1}, \nu_{t+1}, g_{\nu, t+1}$
 - 7: **end for**
 - 8: Update ζ using total SNS estimator loss (Eq. (22)) and α_1
-

Correction step. The estimator applies a correction to the prior using all available information:

$$\begin{aligned} X_t &= \bar{X}_{t|t-1} + d\hat{\mu}_\zeta(\bar{X}_{t|t-1}, U_t, Y_t, \nu_t, g_{\nu, t}) + \varepsilon, \quad \varepsilon \sim \mathcal{C}(0, \hat{\Sigma}) \\ &\approx \hat{\mu}_\zeta(\bar{X}_{t|t-1}, U_t, Y_t, \nu_t, g_{\nu, t}). \end{aligned} \quad (16)$$

Where $\{Y_t : y_{t-H:t} \cap X_t = \emptyset\}$ are the measurement histories that do not overlap with the state histories. This would include, for example, base acceleration. For directly measurable state components (e.g., joint angles and velocities), we fill the corresponding entries of $\bar{X}_{t|t}$ with their noise corrupted sensor readings rather than a learned correction. In other words, the estimator is only trained to estimate unmeasurable or “privileged” states while noisy measurements/states are used without correction.

Loss functions and concurrent training. We train the dynamics model and estimator *concurrently*, with each module receiving its own loss while also influencing the other’s inputs during rollout. This is not unlike concurrent methods in model-free RL [63]. Table III gives a high-level overview of the role of each loss, while Algorithms 2 and 3 detail how the losses are computed during training.

The dynamics model is trained with

$$\mathcal{L}_{\text{dynamics}} = \lambda_0 \mathcal{L}_{\text{step}} + \lambda_1 \mathcal{L}_{\text{rollout}} + \lambda_2 \mathcal{L}_{\text{corrupt}} + \lambda_3 \mathcal{L}_{k\text{-SNS}}. \quad (17)$$

For robust optimization under heavy-tailed residuals we use the mean Cauchy error (MCE)

$$\mathcal{L}_{\text{MCE}} \propto -\log \mathcal{C}(x_{t+1}; \hat{\mu}_\theta, \hat{\Sigma}_{\mathcal{D}}), \quad (18)$$

TABLE III
LOSS COMPONENTS FOR DYNAMICS AND ESTIMATION

Loss Term	Purpose
$\mathcal{L}_{\text{step}}$	One-step predictions
$\mathcal{L}_{\text{rollout}}$	Multi-step predictions
$\mathcal{L}_{\text{corrupt}}$	Robustness to poor state estimates
$\mathcal{L}_{\text{estimator}}$	Multi-step estimation accumulation
$\mathcal{L}_{k\text{-SNS}}$	Smoothness constraints/regularization

with homoscedastic dispersion $\hat{\Sigma}_{\mathcal{D}} = \hat{\sigma}^2 I$ estimated via the replay buffer and the MAD. The same MAD and median values are used for fixed “normalization” and “denormalization” layers for the input and output. In the homoscedastic case, (18) corresponds to dropping the $\log |\Sigma|$ term in (9) and averaging across the state and batch dimensions.

The single-step loss along a trajectory of length T is

$$\mathcal{L}_{\text{step}} = \frac{1}{T} \sum_{t=0}^T \mathcal{L}_{\text{MCE}}(x_{t+1}, \hat{\mu}_\theta, \hat{\Sigma}_{\mathcal{D}}), \quad (19)$$

while the multi-step rollout loss is computed autoregressively with discount γ :

$$\mathcal{L}_{\text{rollout}} = \frac{1}{T-1} \sum_{t=1}^T \mathcal{L}_{\text{MCE}}(x_{t+1}, \hat{\mu}_{\theta, t+1}, \hat{\Sigma}_{\mathcal{D}, \gamma^t}). \quad (20)$$

This prevents long-horizon drift [5], [60]. The corrupted-input loss uses estimator outputs as dynamics inputs:

$$\mathcal{L}_{\text{corrupt}} = \frac{1}{T-1} \sum_{t=1}^T \mathcal{L}_{\text{MCE}}(x_{t+1}, \hat{\mu}_\theta(\text{sg}(\bar{X}_{t|t}), \cdot), \hat{\Sigma}_{\mathcal{D}}) \quad (21)$$

to ensure robustness to poor estimates. The estimates are treated as plain data via the stop gradient operator, $\text{sg}(\cdot)$, to avoid training instability. The algorithm for a full training step of the dynamics model is given in Algorithm 2.

The estimator is trained to converge over time using multi-step rollouts starting from noise-perturbed histories:

$$\begin{aligned} \mathcal{L}_{\text{estimator}} &= \frac{1}{H(T-1)} \sum_{t=1}^T \sum_{h=0}^H \mathcal{L}_{\text{MCE}}(x_{t-h:t}, \hat{\mu}_\zeta(\bar{X}_{t|t-1}, \cdot), \hat{\Sigma}_{\mathcal{D}}) \\ &\quad + \lambda_4 \mathcal{L}_{k\text{-SNS}}. \end{aligned} \quad (22)$$

As before, we detach the estimates to prevent exploding gradients during the rollout. The algorithm for a full training step of the estimator model is given in Algorithm 3.

C. Generalized Gauss-Newton MPC

Our basic single-shooting setup (Eq. 8) allows the use of any general-purpose nonlinear optimizer. As our primary gradient-based strategy, we choose a generalized Gauss–Newton method [66]–[68] for sequential quadratic programming.

We refer to our approach as *gray-box*: aside from requiring differentiability and convex costs, the internal structure of the learned dynamics model is irrelevant to the optimizer. This is in contrast to popular Gauss–Newton trajectory optimizers such as the iterative Quadratic Gauss–Newton (iLQG) [69], which impose specific assumptions on the temporal nature of the dynamics, actions, and cost. While our method is inspired

by iLQG, it does not rely on those structural constraints. In addition to the generalized Gauss–Newton procedure, we incorporate GPU-based acceleration to improve solution times.

We parameterize the action (control) sequence $u_{0:T-1}$ using a set of k knots u_κ :

$$u_t = \text{spline}(u_\kappa)(t), \quad u_\kappa \in \mathbb{R}^{n-k}, \quad k \leq T. \quad (23)$$

This parameterization is common in gradient- and sampling-based methods, as it enforces continuity and physical plausibility while reducing the number of decision variables.

Constraints are handled using an augmented objective following [64], [67]:

$$\min_{u_\kappa} \ell(u_\kappa) + \sum_{i=0}^G \beta_i \log_\delta(g_i(u_\kappa)). \quad (24)$$

Here, $\log_\delta(\cdot)$ denotes a relaxed logarithmic barrier:

$$\log_\delta(g_i) = \begin{cases} -\log(-g_i), & g_i < -\delta_i, \\ -\log \delta_i + \frac{1}{2} \left(\frac{g_i + 2\delta_i}{\delta_i} \right)^2 - \frac{1}{2}, & g_i \geq -\delta_i, \end{cases} \quad (25)$$

The relaxation parameters δ_i and β_i regulate the strength of constraint enforcement. As $\delta_i \rightarrow 0$ and $\beta_i \rightarrow 0$, feasible solutions incur vanishing barrier cost, whereas infeasible solutions diverge. In practice, we keep these parameters fixed for each constraint.

Backward pass / quadratic approximation. In the backward pass, we compute a local descent direction for the spline knots. Let (24) be written as a sum over residuals ε_i :

$$\mathcal{J}(\varepsilon(u_\kappa)) = \sum_{i=0}^R \ell_i(\varepsilon_i(u_\kappa)). \quad (26)$$

Here, “residuals” refers to the per-term objective errors in (26) and should not be conflated with the learned dynamics or state estimation residuals discussed above. We seek an update direction δu_κ at point u_κ^- by solving the subproblem:

$$\min_{\delta u_\kappa} \frac{1}{2} \delta u_\kappa^\top H \delta u_\kappa + q^\top \delta u_\kappa. \quad (27)$$

where the gradient is

$$q = \nabla_{u_\kappa} \mathcal{J}(\varepsilon(u_\kappa^-)) = \left(\frac{\partial \varepsilon}{\partial u_\kappa} \right)^\top \nabla_\varepsilon \mathcal{J}(\varepsilon(u_\kappa^-)). \quad (28)$$

and the GGN Hessian is approximated by

$$\begin{aligned} H &\approx \nabla_{u_\kappa}^2 \mathcal{J}(\varepsilon(u_\kappa^-)) \\ &= \left(\frac{\partial \varepsilon}{\partial u_\kappa} \right)^\top \nabla_\varepsilon^2 \mathcal{J}(\varepsilon(u_\kappa^-)) \left(\frac{\partial \varepsilon}{\partial u_\kappa} \right). \end{aligned} \quad (29)$$

If each $\ell_i(\varepsilon)$ is convex in the residual, then its residual-space Hessian is PSD $\nabla_\varepsilon^2 \mathcal{J}(\varepsilon) \succeq 0$. By congruence, H is also PSD. Then, the linear system

$$H \delta u_\kappa = -q \quad (30)$$

is solved efficiently using Cholesky factorization.

Forward pass / greedy parallel line search. Line search stabilizes updates when the full Gauss-Newton step is unreliable due to nonlinearities in the rollout or cost landscape. In the

TABLE IV
AUGMENTED STATE SPACE, ACTIONS, AND MEASUREMENTS

Quantity	Description
z [m]	Base height above terrain
$r_{\mathcal{W}}^{6D}$ [-]	Continuous 6D base orientation representation [70]
q_J [rad]	Joint positions (12 DoF)
v_J [rad/s]	Joint velocities
v_B [m/s]	Base linear velocity (body frame)
ω_B [rad/s]	Base angular velocity (body frame)
ϕ [m]	Signed distances (23 collision geoms)
y	Measurements [$q_J, v_J, r_{\mathcal{W}}^{6D}, \omega_B, \dot{v}_B$]
\hat{y}	Predicted measurements [$\hat{q}_J, \hat{v}_J, \hat{r}_{\mathcal{W}}^{6D}, \hat{\omega}_B, \Delta \hat{v}_B$]
\dot{v}_B [m/s ²]	Base linear acceleration (body frame)
$\Delta \hat{v}_B$ [m/s ²]	Predicted acceleration $(\hat{v}_{B,t} - \hat{v}_{B,t-1})/dt$
u [rad]	Desired joint positions q_J^d

TABLE V
AUGMENTED STATE SPACE

Quantity	Description
z [m]	Base height above terrain
$r_{\mathcal{W}}^{6D}$ [-]	Continuous 6D base orientation representation [70]
q_J [rad]	Joint positions (12 DoF)
v_J [rad/s]	Joint velocities
v_B [m/s]	Base linear velocity (body frame)
ω_B [rad/s]	Base angular velocity (body frame)
ϕ [m]	Signed distances (23 collision geoms)

forward pass, the control knots are updated along the descent direction with step size $\alpha \in [0, 1]$:

$$u_\kappa^+ = u_\kappa^- + \alpha \delta u_\kappa. \quad (31)$$

The step size is selected by solving

$$\alpha^* = \arg \min_{0 \leq \alpha \leq 1} \mathcal{J}(\varepsilon(u_\kappa^- + \alpha \delta u_\kappa)), \quad (32)$$

with the full nonlinear rollout and cost. We approximate this 1D subproblem using a *greedy parallel line search*: R candidate step sizes α are sampled uniformly in $[0, 1]$, and the corresponding rollout trajectories are evaluated in parallel on GPU:

$$\hat{\mathbf{x}}_{0:T} = \text{vmap}(\text{rollout}_\theta(u_\kappa^- + \alpha \delta u_\kappa))(\alpha). \quad (33)$$

where $\hat{\mathbf{x}}_{0:T} \in \mathbb{R}^{R \times T \times n}$ is the batch of candidate trajectories.

D. Offline Training for Online Behavior Synthesis

States, actions, and measurements. We select states to support downstream planning while remaining compatible with the Lipschitz constraints of our smooth neural surrogate models. The augmented state (Table V) includes standard proprioceptive terms together with a 6D orientation representation $r_{\mathcal{W}}^{6D}$ [70] and the signed distances ϕ from each body geometry to the terrain (visualized in Fig. 8). These distances allow the robot to infer proximity to contact across varying terrain profiles for better awareness and can be used for collision avoidance or gait tracking costs and constraints.

Domain randomization. Signed-distance states become richer when the terrain is varied. We randomize the ground-plane slope by applying a uniformly sampled 3D rotation, creating broad terrain variation without explicit curricula. Combined with the signed-distance representation, this serves as our

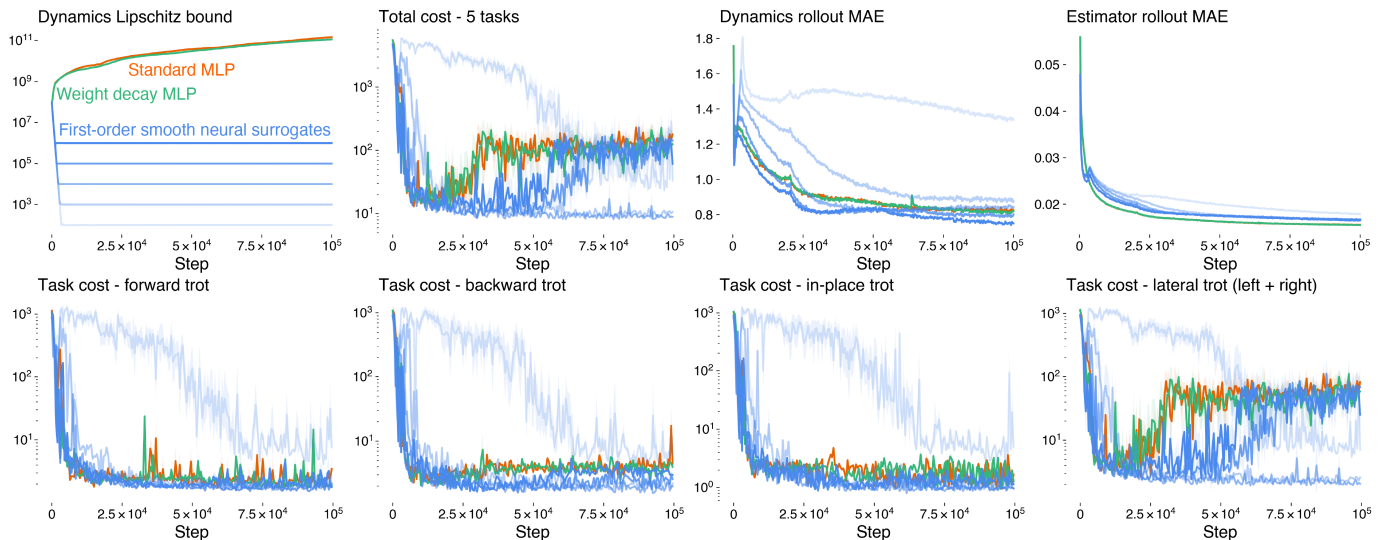


Fig. 9. **Smooth neural surrogates excel at MPC for legged robots.** First-order smooth neural surrogate dynamics with varying Lipschitz constraints are compared to a standard MLP and a weight-decay MLP. Traditional networks become progressively less continuous during training, whereas smooth neural surrogates converge quickly and remain within their prescribed sensitivity budgets. A Pareto trade-off emerges between smoothness and control performance: moderately smooth models perform best for quadruped locomotion. Excessive smoothness slows learning, while insufficient smoothness yields stiff dynamics that degrade planning. Among smooth surrogates, tighter Lipschitz bounds monotonically increases rollout error. Standard and weight-decay MLPs achieve similar rollout error to moderately smooth surrogates but remain unreliable for planning.

TABLE VI
MEASUREMENTS AND CONTROL INPUTS

Quantity	Description
y	Measurements $[q_J, v_J, r_{\mathcal{W}}^{\text{GD}}, \omega_B, \dot{v}_B]$
\hat{y}	Predicted measurements $[\hat{q}_J, \hat{v}_J, \hat{r}_{\mathcal{W}}^{\text{GD}}, \hat{\omega}_B, \Delta \hat{v}_B]$
\dot{v}_B [m/s ²]	Base linear acceleration (body frame)
$\Delta \hat{v}_B$ [m/s ²]	Predicted acceleration $(\hat{v}_{B,t} - \hat{v}_{B,t-1})/dt$
u [rad]	Desired joint positions q_J^d

primary mechanism for encouraging whole-body and terrain awareness (Fig. 8). Although richer terrain models might further improve versatility and sim-to-real transfer, this simple scheme proved sufficient for our purposes. Other robot parameters and initial states are varied during training with full domain randomization; details are provided in Appendix C. **Control costs and constraints.** During training, we intentionally use a simple objective—no gait tracking, no tuned coefficients, and no behavior-specific shaping—to avoid implicit biases toward particular gaits. The reference commands for the base height, orientation, and velocity are randomized to a fixed value that is reset halfway through each episode in each environment (Appendix C). At deployment, locomotion behaviors (trot, bound, pace, gallop, rear, tripod, and transitions) are obtained solely by adding cost terms, imposing constraints, or adjusting weight magnitudes.

VI. EXPERIMENTAL RESULTS

First, we restate our key motivating questions:

- Can smooth neural dynamics and heavy-tailed likelihoods improve training stability and enable reliable gradient-based neural MPC through contact, and what role does each component play in the resulting performance?
- Although sampling-based MPC is often favored under learned neural dynamics, do our design choices also bene-

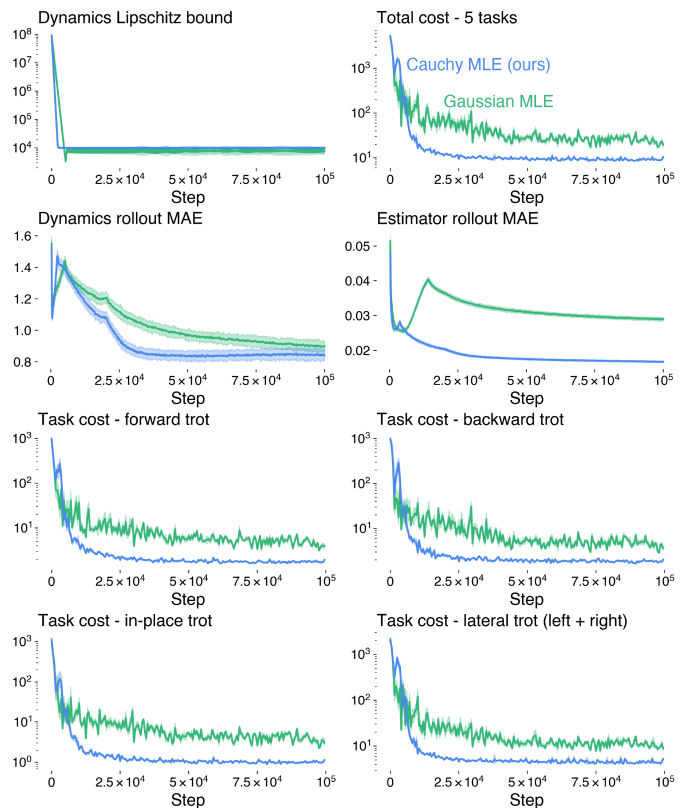


Fig. 10. **Learning with heavy-tailed maximum likelihood estimation improves training stability, motion planning, and model accuracy.** Gaussian MLE, common in model-based RL, fails to capture the error distribution we observe while training stiff legged-robot dynamics. In contrast, heavy-tailed Cauchy MLE yields more stable convergence, higher prediction accuracy, and lower overall control cost. With Cauchy likelihoods we observe $\approx 5\times$ lower cost at 25,000 training steps, shrinking to $\approx 2\text{-}3\times$ lower cost at 100,000 steps.

fit sampling-based methods, and what advantages remain for gradient-based MPC once smoothness is enforced?

- Can learned MPC and state estimation for legged robots combine the versatility afforded by domain randomization with the task-level flexibility of MPC?

We evaluate these questions through online quadruped behavior synthesis or zero-shot generalization, which we define as executing MPC tasks specified by the cost function, constraints, or environment that lie outside the training distribution. In controlled experiments, we test these motivating questions and our hypothesis that nonsmoothness is a key contributor to poor control performance. We perform targeted ablations to isolate the effects of each design choice and compare them against baselines that ignore the role of smoothness. We also present detailed experiments comparing sampling-based and gradient-based control in the context of learned MPC. Finally, we validate our conclusions through deployment on real hardware. More detailed discussions on the implementations, hyperparameters, and deployment are provided in Appendix C. Complementary experiments are also provided in Appendix D.

A. Convergence Behavior and Basic Control

We first examine how smooth neural surrogates and heavy-tailed likelihoods influence the convergence behavior, training stability, and basic trotting locomotion control. For these experiments, we simply use our gradient-based GGN-MPC (with state estimation) and evaluate the closed-loop cumulative cost over a 5 second episode, averaged over at least 10 seeds (Appendix C). Where applicable, error bars are calculated from the log-transformed data. In this subsection, the training setups are identical except for the independent variable of interest and the learning rate, which is tuned to the best of our ability for each method. First-order smooth neural surrogates and Cauchy likelihoods are used unless otherwise stated.

Lipschitz bounds. Fig. 9 shows how the Lipschitz bounds of MLPs influence training and control. We see that the Lipschitz bounds of standard and weight-decay MLPs grow rapidly during training, and these models perform poorly in control, especially as training continues. SNS-MLPs remain within their sensitivity budgets and exhibit a Pareto front between smoothness and control: overly smooth models learn slowly, loosely bounded models behave like standard MLPs, and moderate bounds work best for planning.

Interestingly, control performance for lateral trotting degrades sharply, which suggests that early stoppage could provide some of the benefits of smoothing. Lateral locomotion is inherently less stable, and this sensitivity likely amplifies the effects of stiff gradients, local overfitting, or nonsmooth behavior. We examine these generalization failures in greater detail in the following subsection. Crucially though, meaningful improvements in closed-loop control beyond 50,000 training steps are only observed for SNS-MLPs with $c_{ub} \leq 10^4$.

Error assumptions. We’ve already shown that the dynamics residuals follow a Cauchy distribution more closely than a Gaussian distribution (Fig. 7). Now, we investigate how the choice of likelihood affects training and control. In the

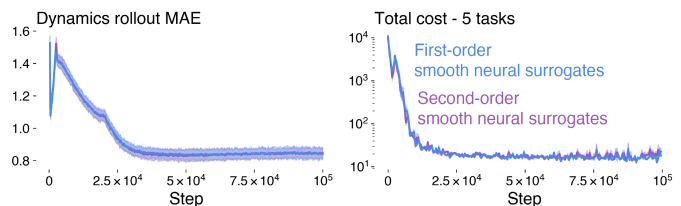


Fig. 11. **First- and second-order smooth neural surrogates.** Both networks achieve comparable prediction and planning performance in our Gauss–Newton MPC setup, as the solver relies on first-order derivatives.

Gaussian case, the Cauchy terms in (17) and (22) are replaced with the mean Mahalanobis error (MME)

$$\mathcal{L}_{\text{MME}} = \frac{1}{nN_{\mathcal{D}}} \sum_{x \in \mathcal{D}} \frac{1}{2} (x - \mu)^{\top} \Sigma^{-1} (x - \mu). \quad (34)$$

The median and MAD are replaced by the mean and standard deviation for the normalization layers and loss calculations. We preserve the scaling for fairness instead of using the more common MSE (i.e., $\mathcal{L}_{\text{MME}}(x, \mu, I)$). Models trained with the heavy-tailed Cauchy likelihood achieve lower prediction error, faster and more stable convergence, and substantially lower control cost than those trained with Gaussian MLE (Fig. 10). This suggests that heavy-tailed residual models are better suited to train supervised models for legged robots, in our setting. Both setups use the same c_{ub} and Lipschitz penalty weights λ_3 and λ_4 . Yet, the dynamics and estimator modules trained with Gaussian Likelihoods struggle to maintain similar smoothness and error levels as the Cauchy-trained modules.

First- and second-order bounds. Lastly, we compare first- and second-order smooth neural surrogates and find that, in our setting, the smoothing order does not substantially influence prediction accuracy or planning performance (Fig. 11). This result could be expected as our generalized Gauss–Newton solver only calculates first-order derivatives through forward simulation. We anticipate that second-order smoothing will be more consequential in settings that rely explicitly on Hessian information such as full Newton methods, or differentiable optimization.

B. Zero-Shot Generalization

We now examine zero-shot generalization in more challenging control scenarios, with the goal of understanding when and why smooth neural surrogates succeed while standard neural networks fail. In particular, we aim to disentangle the effects of model smoothness, likelihood choice, solver type, and state estimation. To this end, each trained model type is evaluated after 100,000 training steps using both sampling-based and gradient-based MPC, with and without learned state estimation. We additionally compare smooth neural surrogates against early-stopped standard MLPs to assess whether observed performance differences arise primarily from reduced overfitting, from smoothness, or from their interaction. Early-stopped standard MLPs are frozen after 12,500 training steps, prior to the onset of any mean control performance degradation over 5 s evaluation episodes (Fig. 9). We use SNS-MLPs with $c_{ub} = 10^4$ and, as previously mentioned, DIAL-MPC [26] is used as a representative sampling-based method.

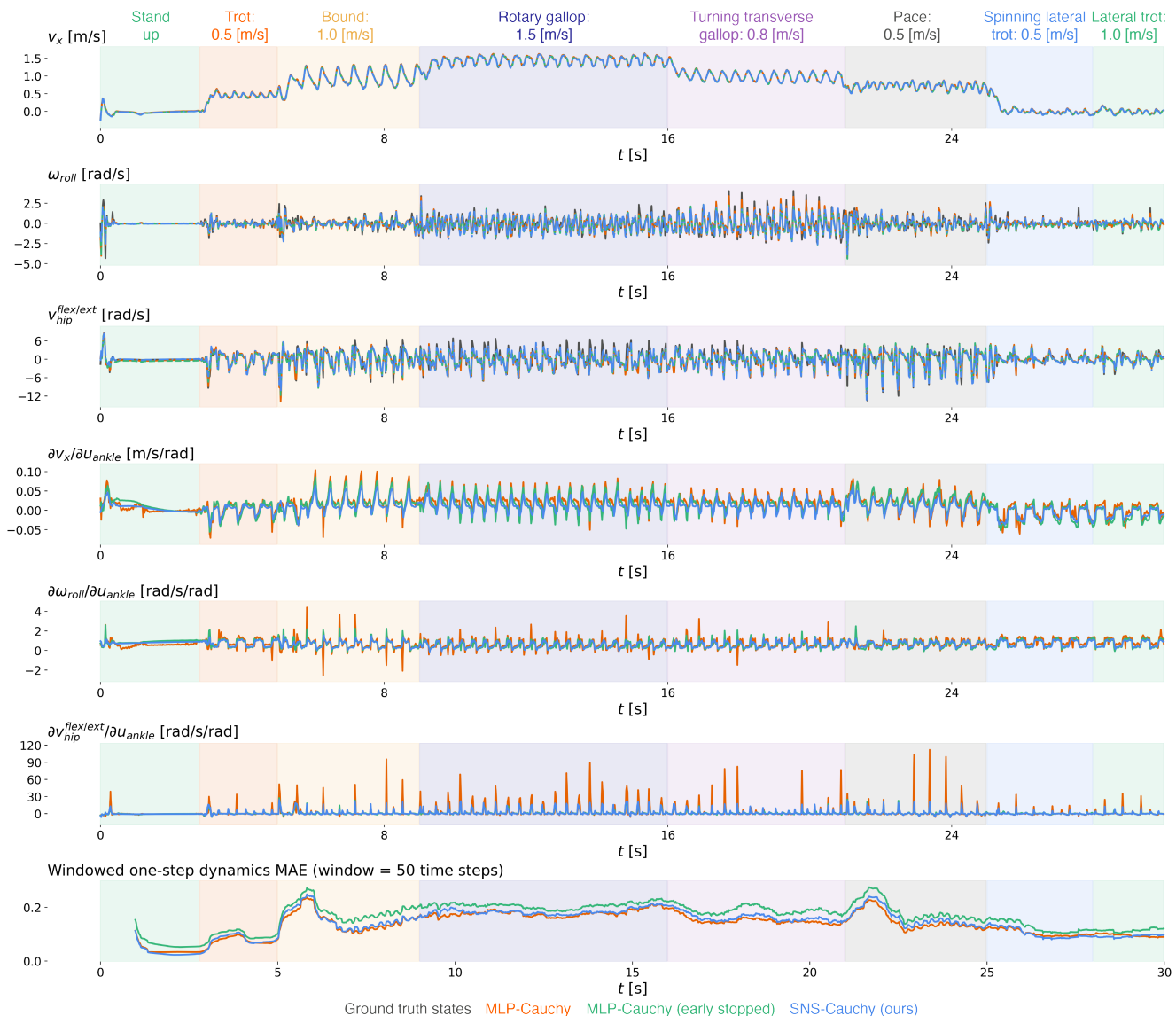


Fig. 12. **First-order model properties correlate with planning performance, while zeroth-order error can be misleading.** Single-step predictions of representative states and their derivatives along a trajectory containing multiple behaviors (listed above). Although the trajectory was generated using an SNS-based controller, predictions from standard MLPs trained with Cauchy likelihoods are also shown to highlight characteristic failure modes (Table VIII). Along the trajectory, the fully trained standard MLP learns stiffer and sharper dynamics, sometimes exhibiting an $\approx 3\times$ larger derivative range than the SNS, and consequently achieves lower overall MAE (SNS: 0.141 ± 0.004 , MLP: 0.136 ± 0.004 , MLP (early stopped): 0.166 ± 0.004), reflecting the nonsmoothness of the ground-truth dynamics. The early-stopped MLP exhibits relatively smoother derivatives and at points is comparable (at first-order) to the smooth neural surrogate. However, because the model is not explicitly constrained to remain smooth, it still develops regions with stiff or noisy derivatives. Moreover, early stopping significantly degrades the zeroth-order predictions. Despite introducing a small modeling bias relative to the fully trained MLP, smooth neural surrogate dynamics maintain globally smooth derivatives and yield substantially better control performance (Table VIII) than either fully trained or early stopped MLPs. Notably, there are sections or tasks where the SNS-MLP attains comparable or lower MAE than the fully trained standard MLP, indicating that smoothing can improve zeroth-order accuracy in addition to gradient attenuation.

Model, likelihood, and solver performance. We begin by comparing test-time dynamics error across model architectures and likelihoods (Table VII). Standard MLPs achieve the lowest one-step prediction error, with Cauchy likelihoods consistently improving performance relative to Gaussian losses. Smooth neural surrogates, by contrast, exhibit a modest increase in test error, reflecting the bias introduced by enforcing global smoothness on inherently nonsmooth contact dynamics.

Because the test dataset is generated using random actions and the training conditions are otherwise identical, one might

expect a lower test error to correspond with improved control performance, particularly for sampling-based MPC. As we show next, this intuition does not hold. Among models with comparable prediction error, continuity and smoothness are far stronger predictors of reliable and generalizable control than zeroth-order accuracy alone.

Table VIII reports cumulative cost and success rates across representative locomotion tasks for all combinations of model, likelihood, solver, and state estimation. Several trends emerge. Standard MLPs trained to completion can execute relatively

TABLE VII
DYNAMICS TEST ERROR FOR DIFFERENT MODELS AND LIKELIHOODS

Method	One-step MAE
MLP–Gaussian	0.540 ± 0.001
MLP–Cauchy (ES)	0.545 ± 0.001
MLP–Cauchy	0.476 ± 0.001
SNS–Gaussian	0.604 ± 0.001
SNS–Cauchy	0.571 ± 0.001

Notes. Cauchy likelihoods reduce error (mean ± 95% CI) across architectures. Smooth neural surrogates introduce bias under nonsmooth dynamics, but yield better performance in both sampling-based and gradient-based MPC. ES denotes early stopping at 12,500 training steps.

stable behaviors, such as in-place or forward trotting, but typically incur higher cost and fail outright on more challenging tasks, including lateral trotting. In multiple cases, standard MLPs also perform substantially worse under gradient-based optimization than under sampling-based MPC, highlighting their sensitivity to poorly conditioned or noisy derivatives. Early-stopped standard MLPs improve performance on some of the more challenging behaviors relative to fully trained models, but this comes at the expense of increased prediction error, leading to degraded performance on some simpler tasks. Moreover, early stopping alone does not prevent catastrophic failures, as early-stopped models still fail at right-trotting.

In contrast, smooth neural surrogates reliably improve performance across both solver classes. When paired with our generalized Gauss–Newton solver, SNS-MLPs achieve uniformly low costs and perfect success rates across all evaluated behaviors. Cauchy likelihoods further enhance robustness, which is particularly noticeable when using state estimation. Moreover, performance using learned state estimates closely matches that obtained with ground-truth states when using SNS-based dynamics and estimation.

Taken together, these results demonstrate that despite exhibiting higher test error, smooth neural surrogates dramatically outperform standard MLPs in both sampling-based and gradient-based control. This discrepancy indicates that model error fails to capture properties critical for closed-loop planning, which is consistent with prior work [5]. The observed behavior suggests a form of overfitting (for control purposes) tied to local nonsmoothness and derivative instability, phenomena that are not detectable through zeroth-order test error alone and are not fully mitigated by early stopping. Accordingly, we observe no setting in which performance degrades when using SNS-MLPs or Cauchy likelihoods. At worst, performance consistently improves by about 10–50%, and with more complex control tasks, these models enable reliable execution (0/5→5/5 success), yielding $\approx 2\text{--}50\times$ reductions in cost.

Overfitting, stiff gradients, or both? In Section IV, we showed in a 2-D shape interpolation example that local nonsmoothness often emerges in regions of sparse data, and it can be linked, in a practical sense, to overfitting. The failure of standard MLP dynamics in several locomotion tasks raises an analogous question here: *do smooth neural surrogates succeed because they attenuate stiff contact dynamics, or because they suppress overfitting-induced local nonsmoothness?*

The test errors reported in Table VII do not suggest that standard MLPs should perform worse in control; if anything, their lower MAE would predict the opposite. To better understand this discrepancy, we analyze model predictions along

a challenging trajectory generated using SNS-MLP dynamics and GGN-MPC (Fig. 12). This trajectory contains multiple gaits and transitions that standard MLPs consistently fail to reproduce when deployed within an MPC loop.

Along this trajectory, the fully trained standard MLP still attains a lower MAE than the SNS-MLP and visually captures many sharp transients and contact events. At the level of zeroth-order predictions, both models appear broadly similar, except for these rapid changes. The key distinction instead emerges at first order: the derivatives of the SNS-MLP remain smooth, bounded, and well-conditioned, whereas those of the fully trained MLP are noisy, stiff, and highly variable. The early-stopped MLP exhibits noticeably smoother derivatives than the fully trained model, consistent with the intuition that continued training leads to sharper dynamics. However, in the absence of an explicit smoothness constraint, early stopping alone does not prevent the emergence of some locally nonsmooth or noisy gradients, and this comes at the cost of substantially higher prediction error.

These observations suggest that smooth neural surrogates provide two complementary advantages for control. First, they mitigate stiffness arising from contact dynamics, yielding gradients that are better suited for optimization. Second, by enforcing global regularity, they suppress local nonsmoothness in regions of the state–action space that are subject to overfitting or rife with local optima. The combination of these effects enables accurate tracking, coordinated whole-body control, and robustness against catastrophic failures, ultimately supporting reliable zero-shot generalization to new behaviors and terrains Fig. 13.

C. Unlocking the Benefits of Gradient-Based MPC

In the previous subsection, we showed that smooth neural surrogates stabilize sampling- and gradient-based MPC. In this section, we examine the practical advantages of gradient-based MPC enabled by our smooth neural dynamics. We compare GGN-MPC to DIAL-MPC [26] under matched MPC formulations, spline-parameterized controls, and identical costs, dynamics, and state estimators, evaluating both solve time and closed-loop performance over full episodes.

Overall performance and sensitivity to hyperparameters. GGN-MPC and DIAL-MPC share the number of rollouts as a key forward-pass hyperparameter. DIAL-MPC samples candidates from an annealed isotropic Gaussian, while GGN-MPC evaluates deterministic proposals along the descent direction from the backward pass. Although sampling-based MPC improves with more rollouts, Fig. 14 shows that GGN-MPC selects far more informative candidates, achieving low cost with an order of magnitude fewer evaluations. As a result, its cumulative control cost remains significantly lower across all tested numbers of rollouts. GGN-MPC also gains little from additional iterations, whereas DIAL-MPC depends heavily on repeated solves. A single DIAL-MPC iteration is faster, but multiple iterations are required for convergence, reducing overall efficiency. So, we observe about $2\times$ lower cumulative cost at equal, and realistic, solve times.

Scalability. We compare scalability along two axes: the dimensionality of the decision vector and parallelization across

TABLE VIII
MODEL, LIKELIHOOD, AND OPTIMIZER PERFORMANCE ACROSS SAMPLE BEHAVIORS AT TEST-TIME

Method	In-place trot	Forward trot (1 [m/s])	Left trot (1 [m/s])	Forward gallop (1.5 [m/s])
MLP–Gaussian–DIAL	7.05±0.40 / 7.16±0.41 (5/5) / (5/5)	10.44±0.61 / 10.78±1.12 (5/5) / (5/5)	44.80±15.72 / 208.46±277.71 (0/5) / (0/5)	24.54±0.95 / 26.67±1.26 (5/5) / (5/5)
MLP–Gaussian–GGN	9.62±2.40 / 8.57±1.89 (5/5) / (5/5)	5.15±3.19 / 14.50±23.18 (5/5) / (5/5)	301.00±74.40 / 392.49±311.24 (0/5) / (0/5)	33.35±3.62 / 34.84±4.45 (0/5) / (0/5)
SNS–Gaussian–DIAL	6.21±0.19 / 21.70±17.41 (5/5) / (5/5)	8.50±0.54 / 24.70±9.32 (5/5) / (5/5)	203.78±313.91 / 26.75±2.77 (4/5) / (5/5)	30.53±4.27 / 49.83±8.46 (3/5) / (5/5)
SNS–Gaussian–GGN	2.09±0.01 / 10.85±0.65 (5/5) / (5/5)	3.87±0.03 / 13.49±0.28 (5/5) / (5/5)	4.67±0.06 / 22.53±1.04 (5/5) / (5/5)	17.13±2.10 / 35.96±1.94 (5/5) / (5/5)
MLP–Cauchy–DIAL (early stopped)	6.77±0.30 / 11.34±1.84 (5/5) / (5/5)	11.97±0.86 / 15.35±3.23 (5/5) / (5/5)	33.33±13.47 / 27.67±9.60 (2/5) / (4/5)	27.39±1.01 / 33.91±6.86 (4/5) / (3/5)
MLP–Cauchy–GGN (early stopped)	2.19±0.01 / 3.19±0.05 (5/5) / (5/5)	4.40±0.06 / 5.59±0.16 (5/5) / (5/5)	4.34±0.04 / 5.37±0.02 *(5/5) / (5/5)	23.02±2.81 / 21.38±1.82 (0/5) / (2/5)
MLP–Cauchy–DIAL	6.29±0.26 / 6.15±0.21 (5/5) / (5/5)	20.10±12.01 / 31.68±56.19 (4/5) / (1/5)	207.25±171.04 / 174.35±290.23 (0/5) / (0/5)	27.34±8.39 / 54.49±46.58 (4/5) / (2/5)
MLP–Cauchy–GGN	2.54±0.03 / 2.57±0.03 (5/5) / (5/5)	3.86±0.02 / 3.90±0.03 (5/5) / (5/5)	256.43±433.35 / 158.78±76.79 (0/5) / (0/5)	53.27±14.94 / 53.34±22.85 (0/5) / (0/5)
SNS–Cauchy–DIAL	5.93±0.24 / 5.91±0.23 (5/5) / (5/5)	7.62±0.29 / 7.98±0.40 (5/5) / (5/5)	15.66±1.40 / 17.11±0.73 (5/5) / (5/5)	24.94±1.07 / 25.44±1.18 (5/5) / (5/5)
SNS–Cauchy–GGN	1.87±0.01 / 1.99±0.02 (5/5) / (5/5)	3.46±0.03 / 3.69±0.03 (5/5) / (5/5)	3.99±0.02 / 4.10±0.01 (5/5) / (5/5)	15.35±0.11 / 15.65±0.18 (5/5) / (5/5)

Notes. Each entry reports the cumulative cost and success rate over 11 second episodes (Top: **mean** ± **95% CI**. Bottom: (**success rate**)), shown as **GT / Est** corresponding to evaluation with ground-truth states and with learned state estimation, respectively. A trial is counted as **successful** if the robot avoids any undesired contact between the ground and the **base or hips** for the full episode. Method names follow the convention **NN–Likelihood–Optimizer**, where MLP denotes a standard MLP and SNS denotes our proposed smooth neural surrogate (SNS-MLP); Gaussian or Cauchy indicates the training likelihood; and DIAL or GGN denotes sampling-based DIAL-MPC [26] and our gradient-based generalized Gauss–Newton (GGN) solver. Early stopping occurred at 12,500 training steps. During these trials, DIAL-MPC had a solve time of ≈ 11.5 ms per control step, while GGN-MPC required ≈ 8.0 ms per solve. * **Right-trot note.** For brevity, only left-trot results are reported for all methods. In right-trot, MLP–Cauchy–GGN (early stopped) achieved success rates of (3/5) / (0/5), while SNS–Cauchy–GGN achieved (5/5) / (5/5).



Fig. 13. **High-coordination (blind) behaviors synthesized without task or environment specific training using smooth neural surrogates and GGN-MPC.** **Left:** Stable balance in the rearing position. **Middle:** Rotary gallop over rough terrain at 1.5 meters per second. **Right:** Three-legged locomotion.

environments during RL training. In our setup, DIAL-MPC is run for four iterations with 128 rollouts per iteration, whereas GGN-MPC uses a single iteration with only 16 rollouts. As shown in Fig. 15, both methods initially benefit from increasing the action-trajectory resolution, reaching peak performance at roughly ten spline knots (≈ 120 decision variables). Beyond this point, DIAL-MPC degrades rapidly. This is an instance of the curse of dimensionality that is characteristic of sampling-based methods. GGN-MPC, exhibits quadratic growth in solve time due to Cholesky factorization but remains faster at all but the highest resolutions. GGN-MPC also sustains very low costs with high-dimensional decision variables where DIAL-MPC fails, despite using only a single iteration. Overall, this corresponds to $\approx 10\times$ lower cumulative cost at about 300 decision variables.

Parallelization is the cornerstone of large-scale RL. Our JAX implementation parallelizes the optimizers across environments using vectorized mapping $\text{vmap}(\text{MPC}_\theta)$. Because

GGN-MPC requires significantly fewer rollouts and thus less computation per agent, it scales more effectively in GPU-based parallel training, as illustrated in Fig. 15. This results in about $7\times$ faster solves at 1028 environments.

D. Hardware Deployment

Using a single dynamics model and state estimator trained offline and frozen at test time, we generate a wide range of whole-body behaviors by modifying the costs, constraints, and commands online (Fig. 1). Our use of domain randomization during training, together with signed-distance state augmentation, enables robust terrain- and body-aware planning. As shown in Fig. 8, our MPC maintains accurate collision awareness and contact reasoning across uneven slopes, slippery surfaces, and deep debris, and reliably recovers from disturbances such as falls.

Indoors, the same dynamics and estimator produce diverse locomotion patterns—including bounding, galloping, load-

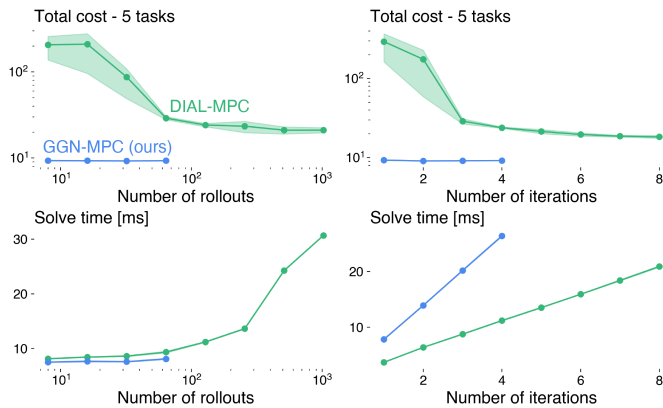


Fig. 14. **Convergence and computational efficiency: gradient-based vs. sampling-based MPC with SNS.** Overall we observe $\approx 2\times$ lower cost at equal solve times when using a fixed, modest, number of action knots ($k = 5$). **Left:** With a fixed iteration count (4 for DIAL-MPC, 1 for GGN-MPC), DIAL-MPC performance depends strongly on rollout count, while GGN-MPC remains consistently low-cost. **Right:** With a fixed rollout count (128 vs. 16), GGN-MPC shows diminishing returns from additional iterations, whereas DIAL-MPC requires more iterations and still fails to reach comparable cost.

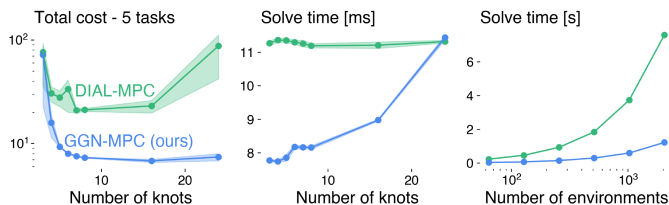


Fig. 15. **Scalability: gradient-based vs. sampling-based MPC with SNS.** **Left:** GGN-MPC maintains low cost across action-trajectory resolutions; DIAL-MPC fails as dimensionality increases ($\approx 10\times$ lower cost at 24 knots). **Middle:** GGN-MPC solve time grows quadratically with knots yet remains efficient and achieves much lower mean cost. **Right:** In parallel environments, sampling-based MPC scales poorly due to large rollout requirements, while GGN-MPC remains more efficient ($\approx 7\times$ faster at 1028 environments).

carrying, and multi-directional push recovery (Fig. 16). We take advantage of the task-level flexibility of MPC, refining behavior quality through cost tuning to correct for failure modes such as high-speed deceleration (Fig. 17). Because we explicitly incorporate behavior stitching (Appendix C), the controller transitions smoothly between gaits with different costs and constraints (Fig. 18), without explicitly training for this behavior. Together, these results demonstrate that our offline-learned smooth neural dynamics, when combined with online MPC, enable flexible, robust, and versatile behavior generation in the real world.

VII. CONCLUSION

This work examined whether learned dynamics models can support reliable, task-flexible MPC for legged robots despite the discontinuities and stiffness induced by contact. We showed that standard neural networks reproduce many of the same numerical pathologies that hinder classical trajectory optimization under contact, while introducing additional failure modes due to local nonsmoothness and overfitting. These observations motivated the smooth neural surrogate MLP, a lightweight yet scalable architecture with tunable

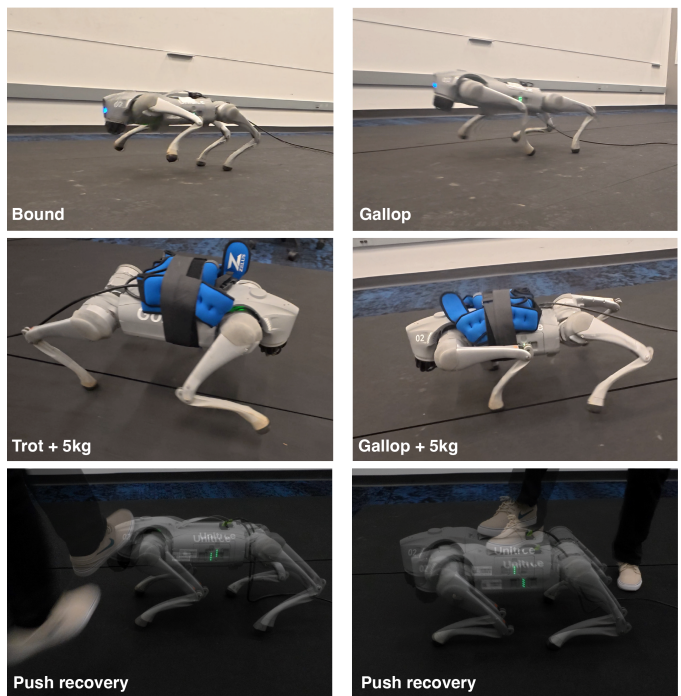


Fig. 16. **Sample indoor experiments.** **Top:** Bounding and galloping gaits. **Middle:** Locomotion with external payload. **Bottom:** Push recovery.



Fig. 17. **Cost tuning on hardware.** The standing controller, which is engaged when no velocity is commanded, is not tested in simulation; instead, we begin with the trotting cost using a zero commanded foot height. This formulation fails to decelerate the robot at high speeds because it over-penalizes stepping and under-penalizes orientation and height tracking, causing the robot to fall by not taking an extra stabilizing step. After adjusting these weights, the controller achieves stable deceleration from sprinting.

first- and second-order gradient bounds, paired with a heavy-tailed training objective that better reflects the impulse-like distribution of model errors observed in legged robots.

Across controlled simulation studies and hardware experiments, smooth neural surrogates yielded substantially more informative derivatives and improved regularity in the learned dynamics, benefiting both sampling-based and gradient-based optimization. When combined with a smooth learned estimator and domain randomization, a single frozen model was sufficient to synthesize a wide range of legged behaviors at test time, including locomotion over uneven terrain and multi-gait transitions, without behavior-specific training or finetuning.

Taken together, our results suggest that relatively simple architectural and training choices can substantially improve the compatibility between learned dynamics and model-based planners. This provides a practical and scalable alternative to hand-designed models and standard model-based RL pipelines

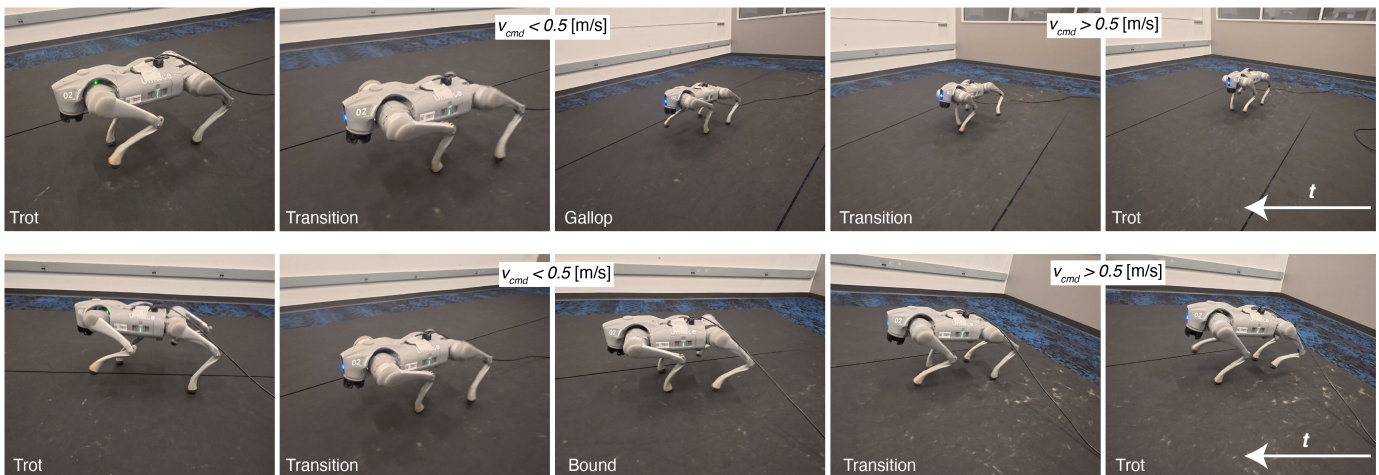


Fig. 18. **Swapping costs and constraints in real time.** At each control step, the MPC solves a distinct objective. Low velocity commands use the default trotting cost, while crossing the 0.5 m/s threshold triggers the transition cost, which provides no explicit gait reference and allows the controller to plan its own steps between gaits. **Top:** For velocity commands above 0.5 m/s, the controller blends the transition cost with the galloping objective using an exponential moving average. **Bottom:** Similarly, velocity commands above 0.5 m/s blend the transition cost with the bounding objective.

TABLE IX
COST TERMS AND WEIGHTS USED FOR NEURAL MPC ON THE GO2 QUADRUPED ACROSS BEHAVIORS

Name	Cost Term	Equation	Training	Trot	Bound/Gallop	Pace	Tripod	Transition	Stand	Weight
Base orientation tracking		$\ \log(\hat{R}_W^T R_W^{\text{cmd}})\ ^2$	1	1	0.65	1	0.7	EMA	2	
Base height tracking		$\ \hat{z} - z^{\text{cmd}}\ ^2$	5	5	1.25	5	0.5	EMA	6	
Base linear velocity tracking		$\ \hat{v}_B - v_B^{\text{cmd}}\ ^2$	$3 \cdot 10^{-2}$	$5 \cdot 10^{-2}$	$5 \cdot 10^{-2}$	$5 \cdot 10^{-2}$	$5 \cdot 10^{-2 \dagger \dagger}$	EMA	$5 \cdot 10^{-2}$	
Base angular velocity tracking		$\ \hat{\omega}_B - \omega_B^{\text{cmd}}\ ^2$	10^{-3}	10^{-3}	$5 \cdot 10^{-4}$	10^{-3}	$5 \cdot 10^{-4 \ddagger}$	EMA	10^{-3}	
Gait / foot height tracking		$\ \hat{\phi}_{\text{foot}} - \phi_{\text{foot}}^{\text{cmd}}\ ^2$	0	2	7	4	7^\dagger	Prev.	0.5	
Nominal joint position penalty		$\ \hat{q}_J - q_J^{\text{nom}}\ ^2$	10^{-2}	10^{-2}	10^{-2}	10^{-2}	10^{-2}	$5 \cdot 10^{-4}$	10^{-2}	
Joint velocity penalty		$\ \hat{v}_J\ ^2$	10^{-8}	10^{-2}	$5 \cdot 10^{-8}$	10^{-2}	$5 \cdot 10^{-8}$	10^{-6}	10^{-2}	
Torque penalty		$\ \hat{\tau}\ ^2$	$2 \cdot 10^{-6}$	$4 \cdot 10^{-6}$	$4 \cdot 10^{-6}$	$4 \cdot 10^{-6}$	$4 \cdot 10^{-6}$	$4 \cdot 10^{-6}$	$4 \cdot 10^{-6}$	$4 \cdot 10^{-6}$
Pos. mech. work penalty		$\ \max(0, \hat{\tau} \cdot \hat{v}_J)\ ^2$	0	10^{-6}	10^{-6}	10^{-6}	10^{-6}	EMA	10^{-6}	
Drift penalty*		$\ \sum_{t=0}^T (\hat{v}_{xy}(t) - v_{xy}^{\text{cmd}}(t)) dt\ ^2$	0	10^{-5}	10^{-5}	10^{-5}	10^{-5}	EMA	10^{-5}	

Notes. All costs are stagewise unless marked with *, which denotes a trajectory-level (global) cost. The global cost is used during the MPC solve but excluded when evaluating the closed-loop control cost. \dagger : FR foot has a weight of 35. $\dagger\dagger$: Velocity v_y as a weight of 25. \ddagger : Angular velocity ω_z as a weight of 25. EMA indicates that an exponential moving average of the previous task weights and the next commanded task weights are used to determine the current value.

and points toward more flexible, general-purpose controllers for real-world legged robots.

Limitations and future work. While effective for quadruped locomotion, several extensions remain open. Applying smooth neural surrogates to contact-rich manipulation and humanoid robots may enable more general whole-body control. Incorporating smooth surrogates into policy learning pipelines could stabilize gradient-based updates by providing better-conditioned or adaptive model derivatives. Integrating raw perceptual inputs such as vision, depth, or tactile sensing into both the dynamics and estimator models would further improve terrain awareness and planning under partial observability. Finally, although Lipschitz constraints have been proposed for more expressive architectures such as CNNs and transformers, their practical benefits in high-capacity networks for robotics and control remain largely unexplored.

These directions suggest that smooth neural surrogates may serve as modular building blocks that enhance a broad class of scalable, contact-rich learning and control methods.

ACKNOWLEDGMENTS

This work was supported by the National Science Foundation Graduate Research Fellowship, by ARO under award W911NF2410405, and by DARPA TIAMAT program under award HR00112490419.

APPENDIX A

CURVATURE BOUND ON SMOOTH NEURAL SURROGATE

Proposition. Let $f = f_L \circ \dots \circ f_1$ be a composition of L twice continuously differentiable mappings. For each layer define

$$c_\ell := \sup_x \|Df_\ell(x)\|_p, \quad L_2(f_\ell) := \sup_x \|D^2 f_\ell(x)\|_p. \quad (35)$$

Assume *layerwise 2-smoothness*: there exists a constant $\alpha_2 > 0$ such that

$$L_2(f_\ell) \leq \alpha_2 c_\ell^2 \quad \forall \ell. \quad (36)$$

Then the composition satisfies

$$L_2(f) \leq \alpha_2 \left(\prod_{j=1}^L c_j \right) \sum_{\ell=1}^L c_\ell \prod_{j < \ell} c_j. \quad (37)$$

Proof. Let $h_\ell = f_\ell \circ \dots \circ f_1$. By the chain rule,

$$Df(x) = J_{f_L}(h_{L-1}(x)) \cdots J_{f_1}(x). \quad (38)$$

Differentiating again yields

$$D^2 f(x) = \sum_{\ell=1}^L A_\ell D^2 f_\ell(h_{\ell-1}(x)) \circ (T_\ell, T_\ell), \quad (39)$$

where

$$A_\ell = J_{f_L} \cdots J_{f_{\ell+1}}, \quad T_\ell = J_{f_{\ell-1}} \cdots J_{f_1}, \quad (40)$$

where $(T_\ell, T_\ell) : (u, v) \mapsto (T_\ell u, T_\ell v)$ and $D^2 f_\ell(x)$ is a bilinear form. Thus

$$(D^2 f_\ell(x) \circ (T_\ell, T_\ell))(u, v) = D^2 f_\ell(x)(T_\ell u, T_\ell v), \quad (41)$$

which is the pullback of the Hessian by the linear map T_ℓ . Using submultiplicativity $\|AB\| \leq \|A\| \|B\|$ of the operator norm and the bound $\|B \circ (T_\ell, T_\ell)\| \leq \|B\| \|T_\ell\|^2$, we obtain

$$\|A_\ell D^2 f_\ell(T_\ell, T_\ell)\| \leq \|A_\ell\| \|D^2 f_\ell\| \|T_\ell\|^2. \quad (42)$$

Since $\|J_{f_j}\| \leq c_j$,

$$\|A_\ell\| \leq \prod_{j>\ell} c_j, \quad \|T_\ell\| \leq \prod_{j<\ell} c_j. \quad (43)$$

Layerwise 2-smoothness provides $\|D^2 f_\ell\| \leq \alpha_2 c_\ell^2$. Hence each summand of (39) is bounded by

$$\alpha_2 \left(\prod_{j>\ell} c_j \right) c_\ell^2 \left(\prod_{j<\ell} c_j \right)^2. \quad (44)$$

Factor out the full product $\prod_{j=1}^L c_j$:

$$\left(\prod_{j>\ell} c_j \right) c_\ell^2 \left(\prod_{j<\ell} c_j \right)^2 = \left(\prod_{j=1}^L c_j \right) \left(c_\ell \prod_{j<\ell} c_j \right). \quad (45)$$

Then, summing over ℓ and taking a supremum over x gives

$$L_2(f) \leq \alpha_2 \left(\prod_{j=1}^L c_j \right) \sum_{\ell=1}^L c_\ell \prod_{j<\ell} c_j, \quad (46)$$

which completes the proof.

APPENDIX B SMOOTH NEURAL SURROGATE EXPERIMENTS AND IMPLEMENTATION DETAILS

JAX implementation. The key routine is the normalization function, as in (3), but with our exponential parameterization:

```
import jax.numpy as jnp
def normalization(Wi, theta_ci):
    ci = jnp.exp(theta_ci) # Ours
    #ci = softplus(theta_ci) Liu et.al. (2022)
    absrowsum = jnp.sum(jnp.abs(Wi), axis=1)
    scale = jnp.minimum(1.0, ci/absrowsum)
    return Wi * scale[:,None]
```

As noted in (3), the function rescales the networks weights to satisfy a learned Lipschitz bound. Each layer of the surrogate network then applies this normalization on the forward pass before multiplying by the weight matrix, adds the bias, and passes the result through a nonlinear activation function:

```
def sns_layer(Wi, bi, theta_ci, x):
    Wi_clip = normalization(Wi, theta_ci)
    return act(jnp.dot(Wi_clip, x) + bi)
```

Curvature budget selection. For second-order smoothness, we construct a curvature budget d_{ub} from the same first-order budget. Although d_{ub} could be chosen independently of c_{ub} , we scale it consistently to compare first- and second-order constraints under similar regularization strength (i.e., Fig. 11). We define

$$d_{\text{ub}} = c_{\text{ub}} \sum_{\ell=1}^L c_{\text{ub}}^{\ell/L}, \quad (47)$$

which corresponds to the curvature bound that would arise if all layers shared equal Lipschitz constants $c_{\text{ub}}^{1/L}$. This construction does not enforce equality across layers; it simply provides a consistent scaling.

2-D shape interpolation. We train neural signed-distance functions in (x, y) conditioned on a latent variable z , yielding $d \approx f_\theta(x, y, z)$. The standard MLP uses an MSE loss, and the SNS and Lipschitz MLPs include a first-order smoothness constraint with $c_{\text{ub}} = 8.0$. Our dataset contains 500K uniformly sampled points per shape. All networks use softplus activations, five hidden layers with 192 units, and we train them for 200 epochs with a learning rate of 0.003.

1-D nonsmooth functions. For Fig. 4 and 5, we train on 15K uniformly sampled (x, y) pairs with $y \approx f_\theta(x)$ using an MSE loss. We train the ReLU example for 3000 epochs with $c_{\text{ub}} = 1.0$, and the nonsmooth-objective example for 1000 epochs with $c_{\text{ub}} = 1.35$ and $\lambda = 0.1$. Both models use softplus activations, four hidden layers with 64 units, and a learning rate of 0.01. The nonsmooth function (Fig. 5) is defined as

$$f(x) = \begin{cases} -0.6x - 2.0, & x < -3, \\ -0.2, & -3 \leq x < 1, \\ -0.6, & 1 \leq x < 1.3, \\ -0.6 + 0.8(x - 1.3)^2, & 1.3 \leq x < 2.2, \\ mx + b, & x \geq 2.2, \end{cases} \quad (48)$$

where the coefficients m and b are chosen so that the final segment connects to the quadratic segment at $x = 2.2$ and satisfies $f(5) = 1$.

Smoothing particle-mass contact dynamics. We generate 500 trajectories (6 s at 50 Hz) from random initial states $x_0 = [q_0, v_0] \sim [\mathcal{U}(0.1, 4.0), \mathcal{U}(-5.0, 5.0)]$ under sinusoidal forcing $u_t = 2g \sin(2\pi\omega t)$, $\omega \sim \mathcal{U}(0.1, 3.0)$. The dynamics follow $\ddot{q} = -g + u$ with inelastic collisions at $q = 0$. Models are trained with a single-step MSE loss $x_{t+1} \approx x_t + f_\theta(x_t, u_t)$, dt using Softplus networks with five hidden layers of 192 units, for 500 epochs at a learning rate of 10^{-3} , with $c_{\text{ub}} = 50$ and $\lambda = 0.2$.

APPENDIX C IMPLEMENTATION DETAILS FOR QUADRUPED EXPERIMENTS

This appendix summarizes the simulation environments, data collection pipeline, model architectures, training procedures,

TABLE X
DOMAIN RANDOMIZATION DISTRIBUTIONS FOR GO2 QUADRUPED

Quantity	Distribution
Link masses m [kg]	$\mathcal{U}(0.975 m_0, 1.025 m_0)$
Base COM offset [mm]	$\mathcal{U}(\pm 3)$ per axis
Link COM offsets [mm]	$\mathcal{U}(\pm 1)$ per axis
Joint damping [N·m·s/rad]	$\mathcal{U}(0.0, 0.05)$
Joint friction [N·m·s/rad]	$\mathcal{U}(0.0, 0.25)$
Joint armature [kg·m ²]	$\mathcal{U}(0, 5 \times 10^{-5})$
Foot radius r [m]	$\mathcal{U}(0.95 r_0, 1.05 r_0)$
Sliding friction μ_{slide}	$\mathcal{U}(0.2, 1.0)$
Rolling/torsional friction	Scaled μ_{slide} , clipped to $[0.1, 1.0]$
Terrain tilt axis	Uniform on unit sphere
Terrain tilt angle [rad]	$\mathcal{U}(0, 0.5)$
Latency [ms]	$\mathcal{U}\{10, 15\}$
Measurement noise:	
$r_{\mathcal{W}}^{6D}$	$\mathcal{U}(\pm 0.001)$
q_J [rad]	$\mathcal{U}(\pm 0.01)$
v_J [rad/s]	$\mathcal{U}(\pm 0.1)$
\dot{v}_B [m/s]	$\mathcal{U}(\pm 0.08)$
ω_B [rad/s]	$\mathcal{U}(\pm 0.025)$

costs, constraints, and evaluation protocols used across all quadruped experiments, including simulation studies and real-world deployment. Unless otherwise noted, all settings described below are shared across experiments.

Simulation environments. We run MuJoCo simulation at 200 Hz and perform control and data collection at 50 Hz. We keep MuJoCo’s default contact settings, including `impratio=1`, which is known to produce stiff contacts and large derivatives in legged locomotion [35]. These settings ensure that our training data contain the nonsmooth behaviors characteristic of contact dynamics.

At every reset, we randomize physical and terrain parameters as summarized in Table X, including link masses, centers of mass, joint properties, friction coefficients, foot geometry, and measurement noise. The ground-plane slope is randomized by sampling a uniform tilt axis and angle. To deploy for actuator system identification, we train initial models using MuJoCo’s position-actuator interface with gains $K_p \sim \mathcal{U}(23, 27)$ N·m/rad and $K_d \sim \mathcal{U}(2.5, 3.5)$ N·m·s/rad. All collision geometries in the XML are converted to capsules or spheres to maintain accurate signed-distance computations in our MuJoCo version.

Data collection. Each episode lasts 5.12 s (256 control steps), and we simulate 512 environments in parallel. The replay buffer stores 20,480 episodes (≈ 5 M transitions) and cycles in a FIFO manner. Reference commands are varied across episodes and robot states are randomized at every reset. We collect an initial bootstrap buffer using random uniform spline actions between the minimum and maximum action limits, then alternate between collecting on-policy trajectories and updating our models using the replay buffer. The test dataset (Table VII) is generated using the same procedure.

Hybrid simulation and actuator models. Our control pipeline uses hybrid simulation that combines MuJoCo rigid-body dynamics with a smooth neural surrogate actuator model. For all 12 joints, we log torque, commanded position, actual position, and velocity at 200 Hz. Following [1], [71], we train a single shared actuator network and introduce randomized actuation latency.

For each joint j , the actuator predicts torque from histories of joint-position error $q_J^e = q_J - q_J^d$ and joint velocity:

$$\hat{\tau}_j = A_\psi \left(q_{J,t-P:t}^{e,j}, v_{J,t-P:t}^j \right), \quad (49)$$

using $P = 8$ steps of 200 Hz data. A second actuator network is trained on 50 Hz data with $P = 3$ to accurately capture mechanical work and torque penalties (Table IX) during MPC rollouts. These actuator models are shared across all simulation and hardware experiments.

Model training setup. All learned models use Mish activations and are updated 500 times between data-collection episodes using the Lion optimizer [72]. The global loss uses weights $\lambda_0 = \lambda_1 = 0.5$, $\lambda_2 = 0.05$, and smoothness penalties $\lambda_3 = 10.0$, $\lambda_4 = 10^{-5}$. First-order SNS models use sensitivity budgets of 10^4 for dynamics and 1 for the estimator. The estimator noise covariance is initialized as $\frac{1}{2} \Sigma_{\mathcal{D}}$, computed from the initial replay buffer. All models use history length $H = 8$, rollout horizon $T = 19$, and batch size 512 trajectories (Algorithms 2–3).

All simulation experiments are conducted on a Linux server with 256 CPUs and 8 GPUs. Individual experiments use CPU-based multi-threading for MuJoCo and a single GPU per experiment. Checkpoints are saved every 500 training steps.

Network architectures and learning rates. For simulation experiments, we use:

- Cauchy-loss SNS dynamics / estimator: learning rates 0.0008 / 0.0004,
- Gaussian-loss SNS dynamics / estimator: learning rates 0.0004 / 0.0002,
- Standard and weight-decay MLPs: 0.0001 (dynamics) / 0.00005 (estimator).

These models use four hidden layers with widths $2x_0$ (dynamics) and $1.5y_0$ (estimator), where x_0 and y_0 denote input dimensions. All models use history length $H = 8$.

For hardware deployment, we use the same learning rates with four-layer MLPs with widths:

- Dynamics: $[1.5x_0, 1.5x_0, 1.25x_0, 1.0x_0]$,
- Estimator: $[1.5y_0, 1.25y_0, 1.0y_0, 0.75y_0]$.

These architectures incorporate the same smooth-surrogate constraints, and the same trained model is used across all real-world experiments.

Costs and constraints. We use quadratic tracking objectives during training, validation, and deployment, with task-specific weights listed in Table IX. The cost penalizes deviations in base and joint motion, torque effort, gait phase and foot height, and includes a trajectory-drift term to reduce long-horizon bias.

Training intentionally uses a minimal objective, no gait tracking or tuned coefficients, to avoid implicit bias toward particular gaits. Deployment behaviors (trot, bound, pace, gallop, rear, tripod, and transitions) are obtained exclusively by adding cost terms, adding constraints, or adjusting weight magnitudes. Bounding and galloping enforce collision-avoidance constraints on the thigh and upper shank, $\phi_{\text{thigh}}, \phi_{\text{shank}} > 0$, with relaxation $\delta = 5 \cdot 10^{-4}$ and coefficient $\beta = 10^{-3}$. Tripod additionally enforces base-height bounds $-0.02 < \varepsilon_z < 0.08$ m, with $\delta = 0.01$ and $\beta = 1.0$.

Behavior stitching and transitions. Costs, constraints, and commands are regenerated at each time step and appended to the end of the planning horizon, making the trajectory optimization time-varying. Directly applying new gait parameters can lead to jerky motions or catastrophic failures due to poor foot-height commands. To mitigate this, a transition-specific cost (Table IX) is activated whenever the cost definition changes, temporarily suppressing gait-specific tracking and allowing the optimizer to discover a valid transition. All commands and weights are smoothed using an exponential moving average before being appended to the horizon. This mechanism is only used during evaluation and deployment.

Reference commands. A periodic gait generator produces foot-height references $\phi_{\text{foot}}^{\text{cmd}}$ parameterized by cadence, phase, duty ratio, and swing height [4]. In tripod mode, the disabled leg is assigned a fixed 0.1 m foot-height command; during rearing, both rear legs are disabled. Base height varies throughout training and deployment with nominal height $z^{\text{cmd}} = 0.27$. Nominal joint positions are $q_j^{\text{nom}} = [0, 0.9, -1.8] \times 4$.

Training references are randomized using three distributions. Each batch of episodes contains an equal mixture of:

- **Full random commands:** $(v_x, v_y) \sim \mathcal{U}(-2.0, 2.0)$ m/s, $\omega_{\text{yaw}} \sim \mathcal{U}(-\pi, \pi)$ rad/s, $z \sim \mathcal{U}(0.06, 0.8)$ m, roll, pitch, yaw $\sim \mathcal{U}(-\pi, \pi)$.
- **Random locomotion commands:** $(v_x, v_y, \omega_{\text{yaw}})$ as above, $z \sim \mathcal{U}(0.2, 0.35)$ m, roll and pitch fixed to zero.
- **Random pose commands:** Zero velocities, $z \sim \mathcal{U}(0.35, 0.55)$ m, roll $\sim \mathcal{U}(-\pi/4, \pi/4)$, pitch $\sim \mathcal{U}(-\pi/2, \pi/2)$, yaw $\sim \mathcal{U}(-\pi, \pi)$.

Section-specific experiment settings. Results are averaged across either 10 random seeds (Sec. VI-A and VI-C), or 5 random seeds (Sec. VI-B) governing the initial robot state and, for sampling-based methods, control samples.

Convergence experiments (Sec. VI-A). Linear splines with $k = 5$ knots and 16 rollouts are used with GGN-MPC. Fig. 10, and 11 additionally display results across four independently trained networks per configuration.

Zero-shot generalization (Sec. VI-B). Four models (different seeds) are trained to completion for each network configuration. Models shown in Tables VII and VIII are selected based on trotting performance at the end of training. The early-stopped model is frozen at the 12,500-step checkpoint. For Fig. 12, Fig. 13, and Table VIII, we use $k = 6$ knots and 16 rollouts.

Gradient-based MPC comparisons (Sec. VI-C). The same SNS-Cauchy models from Sec. VI-B are used to evaluate GGN-MPC and DIAL-MPC across five trotting tasks (identical to Sec. VI-A).

Hardware deployment. All deployment algorithms run on a Linux workstation with an Nvidia 4090 GPU and are deployed to the Unitree Go2 via a wired connection. To convert MPC outputs into joint torques, we combine impedance and feed-forward terms:

$$\begin{aligned} \tau = & K_p(q_J^d - q_J) - K_d v_J \\ & + K_p^{\text{ff}}(q_{J,t+1}^* - q_J) - K_d^{\text{ff}}(v_{J,t+1}^* - v_J), \end{aligned} \quad (50)$$

where starred quantities denote MPC-predicted next-step joint positions and velocities. Deployment uses linear splines with

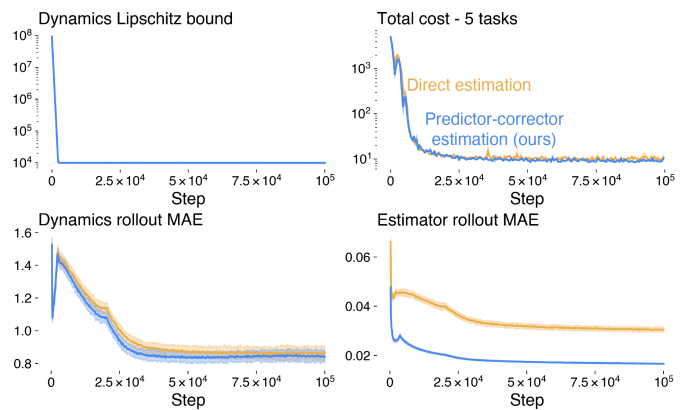


Fig. 19. **Leveraging model predictions for neural estimation.** Direct state-estimation networks, cannot accumulate information over time or leverage predictions from the dynamics model to refine their estimates. In contrast, predictor-corrector strategies accumulate information and integrate model predictions into the estimation loop, yielding more accurate state estimates and lower overall control cost for a quadruped robot.

$k = 6$ knots and GGN-MPC with 8 rollouts per greedy line-search step.

D ADDITIONAL EXPERIMENTS

State estimation. We compared our model-based estimation framework against a direct, model-free estimation strategy [63]. This ablation is not intended to identify the optimal estimator, but rather to demonstrate that derivatives from the smooth neural surrogate can be used to improve estimation quality and downstream control performance. This experiment was conducted under equivalent conditions as the convergence behavior experiments in Section VI-A. The model-free direct estimation approach uses a history of measurements and actions to reconstruct the full state-history:

$$X_t = \bar{\mu}_\zeta(y_{t-H:t}, U_{t-1}) + \varepsilon. \quad (51)$$

For the direct approach, we also assume heavy-tailed errors for ε fair comparison. Fig. 19 shows that our prediction-corrector strategy yields lower and less variable state-estimation error compared to direct estimation. The improved estimation enables faster dynamics learning, as both models are trained jointly. As a result, the total control cost for locomotion also decreases marginally.

Additional hyperparameters. We further demonstrate the sensitivity of sampling-based methods to hyperparameters, as an extension of Section VI-C. Fig. 20 highlights how the performance of DIAL-MPC varies widely with the temperature parameter that governs its softmin reduction, as well as with diffusion-related hyperparameters. In contrast, GGN-MPC applies the lowest-cost candidate directly (equivalent to temperature = 0), has no extra hyperparameters, and remains stable under all tested settings without any regularization (as in Levenberg-Marquardt).

REFERENCES

- [1] J. Lee, J. Hwangbo, L. Wellhausen, V. Koltun, and M. Hutter, “Learning quadrupedal locomotion over challenging terrain,” *Science robotics*, vol. 5, no. 47, p. eabc5986, 2020.

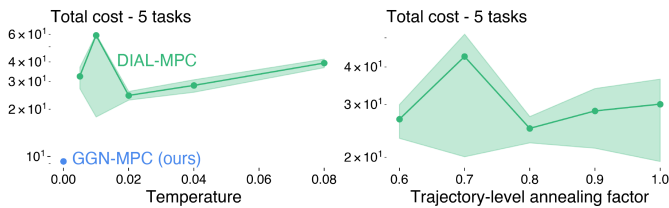


Fig. 20. **Sensitivity to hyperparameters: gradient-based vs. sampling-based MPC with SNS.** **Left:** GGN-MPC is greedy (temperature = 0) and stable. DIAL-MPC performs poorly in the greedy limit and is highly sensitive to temperature. **Right:** Additional diffusion-related hyperparameters further affect DIAL-MPC, whereas our method remains robust without tuning any parameters.

[2] A. Kumar, Z. Fu, D. Pathak, and J. Malik, “Rma: Rapid motor adaptation for legged robots,” *arXiv preprint arXiv:2107.04034*, 2021.

[3] Y. Tassa, T. Erez, and E. Todorov, “Synthesis and stabilization of complex behaviors through online trajectory optimization,” in *2012 IEEE/RSJ International Conference on Intelligent Robots and Systems*. IEEE, 2012, pp. 4906–4913.

[4] T. Howell, N. Gileadi, S. Tunyasuvunakool, K. Zakka, T. Erez, and Y. Tassa, “Predictive sampling: Real-time behaviour synthesis with mujoco,” *arXiv preprint arXiv:2212.00541*, 2022.

[5] M. Lutter, L. Hasenclever, A. Byravan, G. Dulac-Arnold, P. Trochim, N. Heess, J. Merel, and Y. Tassa, “Learning dynamics models for model predictive agents,” *arXiv preprint arXiv:2109.14311*, 2021.

[6] M. Posa and R. Tedrake, “Direct trajectory optimization of rigid body dynamical systems through contact,” in *Algorithmic Foundations of Robotics X: Proceedings of the Tenth Workshop on the Algorithmic Foundations of Robotics*. Springer, 2013, pp. 527–542.

[7] M. Kelly, “An introduction to trajectory optimization: How to do your own direct collocation,” *SIAM review*, vol. 59, no. 4, pp. 849–904, 2017.

[8] G. Kim, D. Kang, J.-H. Kim, S. Hong, and H.-W. Park, “Contact-implicit model predictive control: Controlling diverse quadruped motions without pre-planned contact modes or trajectories,” *The International Journal of Robotics Research*, vol. 44, no. 3, pp. 486–510, 2025.

[9] H.-T. D. Liu, F. Williams, A. Jacobson, S. Fidler, and O. Litany, “Learning smooth neural functions via lipschitz regularization,” in *ACM SIGGRAPH 2022 Conference Proceedings*, 2022, pp. 1–13.

[10] M. Rosca, T. Weber, A. Gretton, and S. Mohamed, “A case for new neural network smoothness constraints,” in *Proceedings on “I Can’t Believe It’s Not Better!” at NeurIPS Workshops*, ser. Proceedings of Machine Learning Research, J. Zosa Forde, F. Ruiz, M. F. Pradier, and A. Schein, Eds., vol. 137. PMLR, 12 Dec 2020, pp. 21–32. [Online]. Available: <https://proceedings.mlr.press/v137/rosca20a.html>

[11] C. Anil, J. Lucas, and R. Grosse, “Sorting out lipschitz function approximation,” in *International conference on machine learning*. PMLR, 2019, pp. 291–301.

[12] I. Gulrajani, F. Ahmed, M. Arjovsky, V. Dumoulin, and A. C. Courville, “Improved training of wasserstein gans,” *Advances in neural information processing systems*, vol. 30, 2017.

[13] Y. Yoshida and T. Miyato, “Spectral norm regularization for improving the generalizability of deep learning,” *arXiv preprint arXiv:1705.10941*, 2017.

[14] X. Song, J. Duan, W. Wang, S. E. Li, C. Chen, B. Cheng, B. Zhang, J. Wei, and X. S. Wang, “Lipsnet: a smooth and robust neural network with adaptive lipschitz constant for high accuracy optimal control,” in *International Conference on Machine Learning*. PMLR, 2023, pp. 32 253–32 272.

[15] W. G. Y. Tan and Z. Wu, “Robust machine learning modeling for predictive control using lipschitz-constrained neural networks,” *Computers & Chemical Engineering*, vol. 180, p. 108466, 2024.

[16] J. Xu, E. Heiden, I. Akinola, D. Fox, M. Macklin, and Y. Narang, “Neural robot dynamics,” *arXiv preprint arXiv:2508.15755*, 2025.

[17] K. Chua, R. Calandra, R. McAllister, and S. Levine, “Deep reinforcement learning in a handful of trials using probabilistic dynamics models,” *Advances in neural information processing systems*, vol. 31, 2018.

[18] J. Amigo, R. Khorrambakhht, E. Chane-Sane, N. Mansard, and L. Righetti, “First order model-based rl through decoupled backpropagation,” *arXiv preprint arXiv:2509.00215*, 2025.

[19] A. Byravan, L. Hasenclever, P. Trochim, M. Mirza, A. D. Ialongo, Y. Tassa, J. T. Springenberg, A. Abdolmaleki, N. Heess, J. Merel

et al., “Evaluating model-based planning and planner amortization for continuous control,” *arXiv preprint arXiv:2110.03363*, 2021.

[20] M. Parmar, M. Halm, and M. Posa, “Fundamental challenges in deep learning for stiff contact dynamics,” in *2021 IEEE/RSJ International Conference on Intelligent Robots and Systems (IROS)*. IEEE, 2021, pp. 5181–5188.

[21] P. Roth, J. Frey, C. Cadena, and M. Hutter, “Learned perceptive forward dynamics model for safe and platform-aware robotic navigation,” *arXiv preprint arXiv:2504.19322*, 2025.

[22] W. Xiao, H. Xue, T. Tao, D. Kalaria, J. M. Dolan, and G. Shi, “Anycar to anywhere: Learning universal dynamics model for agile and adaptive mobility,” in *2025 IEEE International Conference on Robotics and Automation (ICRA)*. IEEE, 2025, pp. 8819–8825.

[23] P. Tsakalides and C. Nikias, “Maximum likelihood localization of sources in noise modeled as a cauchy process,” in *Proceedings of MILCOM’94*. IEEE, 1994, pp. 613–617.

[24] J. Nocedal and S. J. Wright, *Numerical optimization*. Springer, 2006.

[25] M. P. Kelly, “Transcription methods for trajectory optimization: a beginners tutorial,” *arXiv preprint arXiv:1707.00284*, 2017.

[26] H. Xue, C. Pan, Z. Yi, G. Qu, and G. Shi, “Full-order sampling-based mpc for torque-level locomotion control via diffusion-style annealing,” in *2025 IEEE International Conference on Robotics and Automation (ICRA)*. IEEE, 2025, pp. 4974–4981.

[27] E. Lee, S. A. Moore, and B. Chen, “Sym2real: Symbolic dynamics with residual learning for data-efficient adaptive control,” *arXiv preprint arXiv:2509.15412*, 2025.

[28] A. Nagabandi, K. Konolige, S. Levine, and V. Kumar, “Deep dynamics models for learning dexterous manipulation,” in *Conference on robot learning*. PMLR, 2020, pp. 1101–1112.

[29] J. Alvarez-Padilla, J. Z. Zhang, S. Kwok, J. M. Dolan, and Z. Manchester, “Real-time whole-body control of legged robots with model-predictive path integral control,” in *2025 IEEE International Conference on Robotics and Automation (ICRA)*. IEEE, 2025, pp. 14 721–14 727.

[30] Y. Sun, G. G. Yen, and Z. Yi, “Evolving unsupervised deep neural networks for learning meaningful representations,” *IEEE Transactions on Evolutionary Computation*, vol. 23, no. 1, pp. 89–103, 2018.

[31] M. A. Patterson and A. V. Rao, “Gpops-ii: A matlab software for solving multiple-phase optimal control problems using hp-adaptive gaussian quadrature collocation methods and sparse nonlinear programming,” *ACM Transactions on Mathematical Software (TOMS)*, vol. 41, no. 1, pp. 1–37, 2014.

[32] W.-C. Huang, A. Aydinoglu, W. Jin, and M. Posa, “Adaptive contact-implicit model predictive control with online residual learning,” in *2024 IEEE International Conference on Robotics and Automation (ICRA)*. IEEE, 2024, pp. 5822–5828.

[33] S. Le Cleac’h, T. A. Howell, S. Yang, C.-Y. Lee, J. Zhang, A. Bishop, M. Schwager, and Z. Manchester, “Fast contact-implicit model predictive control,” *IEEE Transactions on Robotics*, vol. 40, pp. 1617–1629, 2024.

[34] T. A. Howell, S. Le Cleac’h, J. Z. Kolter, M. Schwager, and Z. Manchester, “Dojo: A differentiable simulator for robotics,” *arXiv preprint arXiv:2203.00806*, vol. 9, no. 2, p. 4, 2022.

[35] J. Z. Zhang, T. A. Howell, Z. Yi, C. Pan, G. Shi, G. Qu, T. Erez, Y. Tassa, and Z. Manchester, “Whole-body model-predictive control of legged robots with mujoco,” *arXiv preprint arXiv:2503.04613*, 2025.

[36] I. Mordatch, E. Todorov, and Z. Popović, “Discovery of complex behaviors through contact-invariant optimization,” *ACM Transactions on Graphics (ToG)*, vol. 31, no. 4, pp. 1–8, 2012.

[37] T. Erez and E. Todorov, “Trajectory optimization for domains with contacts using inverse dynamics,” in *2012 IEEE/RSJ International conference on intelligent robots and systems*. IEEE, 2012, pp. 4914–4919.

[38] H. J. T. Suh, T. Pang, and R. Tedrake, “Bundled gradients through contact via randomized smoothing,” *IEEE Robotics and Automation Letters*, vol. 7, no. 2, pp. 4000–4007, 2022.

[39] T. Pang, H. T. Suh, L. Yang, and R. Tedrake, “Global planning for contact-rich manipulation via local smoothing of quasi-dynamic contact models,” *IEEE Transactions on robotics*, vol. 39, no. 6, pp. 4691–4711, 2023.

[40] J. Xu, V. Makoviychuk, Y. Narang, F. Ramos, W. Matusik, A. Garg, and M. Macklin, “Accelerated policy learning with parallel differentiable simulation,” *arXiv preprint arXiv:2204.07137*, 2022.

[41] I. Georgiev, K. Srinivasan, J. Xu, E. Heiden, and A. Garg, “Adaptive horizon actor-critic for policy learning in contact-rich differentiable simulation,” *arXiv preprint arXiv:2405.17784*, 2024.

[42] C. Schwarke, V. Klemm, J. Bagajo, J. P. Sleiman, I. Georgiev, J. T. Torres, and M. Hutter, “Learning deployable locomotion control via

- differentiable simulation,” in *9th Annual Conference on Robot Learning*, 2025.
- [43] D. Hafner, T. Lillicrap, J. Ba, and M. Norouzi, “Dream to control: Learning behaviors by latent imagination,” *arXiv preprint arXiv:1912.01603*, 2019.
- [44] M. Janner, J. Fu, M. Zhang, and S. Levine, “When to trust your model: Model-based policy optimization,” *Advances in neural information processing systems*, vol. 32, 2019.
- [45] C. Li, A. Krause, and M. Hutter, “Robotic world model: A neural network simulator for robust policy optimization in robotics,” *arXiv preprint arXiv:2501.10100*, 2025.
- [46] G. Williams, N. Wagener, B. Goldfain, P. Drews, J. M. Rehg, B. Boots, and E. A. Theodorou, “Information theoretic mpc for model-based reinforcement learning,” in *2017 IEEE international conference on robotics and automation (ICRA)*. IEEE, 2017, pp. 1714–1721.
- [47] Y. Hu, B. Chen, and H. Lipson, “Egocentric visual self-modeling for autonomous robot dynamics prediction and adaptation,” *npj Robotics*, vol. 3, no. 1, p. 14, 2025.
- [48] R. Huang, H. Balim, H. Yang, and Y. Du, “Flexible locomotion learning with diffusion model predictive control,” *arXiv preprint arXiv:2510.04234*, 2025.
- [49] S. Pfrommer, M. Halm, and M. Posa, “Contactnets: Learning discontinuous contact dynamics with smooth, implicit representations,” in *Conference on Robot Learning*. PMLR, 2021, pp. 2279–2291.
- [50] A. Hochlehnert, A. Terenin, S. Sæmundsson, and M. Deisenroth, “Learning contact dynamics using physically structured neural networks,” in *International Conference on Artificial Intelligence and Statistics*. PMLR, 2021, pp. 2152–2160.
- [51] M. Lutter, C. Ritter, and J. Peters, “Deep lagrangian networks: Using physics as model prior for deep learning,” *arXiv preprint arXiv:1907.04490*, 2019.
- [52] B. Sukhija, N. Köhler, M. Zamora, S. Zimmermann, S. Curi, A. Krause, and S. Coros, “Gradient-based trajectory optimization with learned dynamics,” *arXiv preprint arXiv:2204.04558*, 2022.
- [53] E. Heiden, D. Millard, E. Coumans, Y. Sheng, and G. S. Sukhatme, “Neuralsim: Augmenting differentiable simulators with neural networks,” in *2021 IEEE International Conference on Robotics and Automation (ICRA)*. IEEE, 2021, pp. 9474–9481.
- [54] T. Miyato, T. Kataoka, M. Koyama, and Y. Yoshida, “Spectral normalization for generative adversarial networks,” *arXiv preprint arXiv:1802.05957*, 2018.
- [55] H. Gouk, E. Frank, B. Pfahringer, and M. J. Cree, “Regularisation of neural networks by enforcing lipschitz continuity,” *Machine Learning*, vol. 110, no. 2, pp. 393–416, 2021.
- [56] X. Qi, J. Wang, Y. Chen, Y. Shi, and L. Zhang, “Lipsformer: Introducing lipschitz continuity to vision transformers,” *arXiv preprint arXiv:2304.09856*, 2023.
- [57] T. Mlotshwa, H. van Deventer, and A. S. Bosman, “Cauchy loss function: Robustness under gaussian and cauchy noise,” in *Southern African Conference for Artificial Intelligence Research*. Springer, 2022, pp. 123–138.
- [58] M. T. El-Melegy, M. H. Essai, and A. A. Ali, “Robust training of artificial feedforward neural networks,” in *Foundations of Computational, Intelligence Volume 1: Learning and Approximation*. Springer, 2009, pp. 217–242.
- [59] J. T. Barron, “A general and adaptive robust loss function,” in *Proceedings of the IEEE/CVF conference on computer vision and pattern recognition*, 2019, pp. 4331–4339.
- [60] S. A. Moore, B. P. Mann, and B. Chen, “Automated global analysis of experimental dynamics through low-dimensional linear embeddings,” *arXiv preprint arXiv:2411.00989*, 2024.
- [61] J.-H. Kim, S. Hong, G. Ji, S. Jeon, J. Hwangbo, J.-H. Oh, and H.-W. Park, “Legged robot state estimation with dynamic contact event information,” *IEEE Robotics and Automation Letters*, vol. 6, no. 4, pp. 6733–6740, 2021.
- [62] R. Hartley, M. Ghaffari, R. M. Eustice, and J. W. Grizzle, “Contact-aided invariant extended kalman filtering for robot state estimation,” *The International Journal of Robotics Research*, vol. 39, no. 4, pp. 402–430, 2020.
- [63] G. Ji, J. Mun, H. Kim, and J. Hwangbo, “Concurrent training of a control policy and a state estimator for dynamic and robust legged locomotion,” *IEEE Robotics and Automation Letters*, vol. 7, no. 2, pp. 4630–4637, 2022.
- [64] G. Kim, Y.-H. Lee, and H.-W. Park, “A learning framework for diverse legged robot locomotion using barrier-based style rewards,” in *2025 IEEE International Conference on Robotics and Automation (ICRA)*. IEEE, 2025, pp. 10 004–10 010.
- [65] G. Revach, N. Shlezinger, X. Ni, A. L. Escoriza, R. J. Van Sloun, and Y. C. Eldar, “Kalmannet: Neural network aided kalman filtering for partially known dynamics,” *IEEE Transactions on Signal Processing*, vol. 70, pp. 1532–1547, 2022.
- [66] N. N. Schraudolph, “Fast curvature matrix-vector products for second-order gradient descent,” *Neural computation*, vol. 14, no. 7, pp. 1723–1738, 2002.
- [67] R. Grandia, F. Jenelten, S. Yang, F. Farshidian, and M. Hutter, “Perceptive locomotion through nonlinear model-predictive control,” *IEEE Transactions on Robotics*, vol. 39, no. 5, pp. 3402–3421, 2023.
- [68] F. Messerer, K. Baumgärtner, and M. Diehl, “Survey of sequential convex programming and generalized gauss-newton methods,” *ESAIM: Proceedings and Surveys*, vol. 71, pp. 64–88, 2021.
- [69] E. Todorov and W. Li, “A generalized iterative lqg method for locally-optimal feedback control of constrained nonlinear stochastic systems,” in *Proceedings of the 2005, American Control Conference, 2005*. IEEE, 2005, pp. 300–306.
- [70] Y. Zhou, C. Barnes, J. Lu, J. Yang, and H. Li, “On the continuity of rotation representations in neural networks,” in *Proceedings of the IEEE/CVF conference on computer vision and pattern recognition*, 2019, pp. 5745–5753.
- [71] G. B. Margolis and P. Agrawal, “Walk these ways: Tuning robot control for generalization with multiplicity of behavior,” in *Conference on Robot Learning*. PMLR, 2023, pp. 22–31.
- [72] X. Chen, C. Liang, D. Huang, E. Real, K. Wang, H. Pham, X. Dong, T. Luong, C.-J. Hsieh, Y. Lu *et al.*, “Symbolic discovery of optimization algorithms,” *Advances in neural information processing systems*, vol. 36, pp. 49 205–49 233, 2023.